



Microscopic origins of shape effects on migration and clogging of fines in porous media using coupled CFD-iDEM

Hao Xiong^{1,2,3} · Zhimin Zhang^{1,2,3} · Zhen-Yu Yin⁴ · Xiangsheng Chen^{1,2,3} · Wanhuan Zhou⁵

Received: 4 April 2023 / Accepted: 24 January 2024
© The Author(s) 2024

Abstract

The unstable mechanical behavior of soil particles during suffusion, including migration and clogging of fine particles in porous media, is prone to induce seepage catastrophes. Mechanical behavior of migratory fines and porous soils during suffusion is significantly influenced by the particle shape, which remains unclear. In this study, a coupled computational fluid dynamics and the irregular discrete element method (CFD-iDEM) framework is developed to investigate the migration and clogging mechanisms. A series of numerical simulations that consider spheres and irregular particles with different levels of aspect ratio are carried out to elucidate the microscopic origins of shape effects on clogging. Migratory fine particles are discharged from the grain inlet and enter the coarse particle skeleton by imposing a downward seepage flow. The subsequent migration and clogging phenomena and microscopic mechanisms are investigated. The results reveal that irregular particles present varying degrees of ability to develop clogging clusters, and spheres are more prone to traverse deeper into soil skeleton. The proposed CFD-iDEM method is able to reproduce macroscopic phenomena of saturated porous medium as well as to analyze microscopic origins of fluid–particle interactions, which contributes to practical guidance for engineering applications.

Keywords Suffusion · Migration and clogging mechanisms · Irregular shape · CFD-DEM

1 Introduction

Recently, with the rapid advancement of urbanization, the construction of numerous underground structures has modified the groundwater seepage conditions frequently. Changes in groundwater flow patterns will cause suffusion in the pores of the aquifer, resulting in a variety of

engineering and environmental disasters [12]. As shown in Fig. 1, rising water levels lead to increased pore water pressure, inducing soil liquefaction, ground softening and leakage from underground structures; downstream lowering of the water table increases the effective stress of soil, and subsidence and even ground collapse are likely to occur under the action of building and vehicle loads [40].

✉ Zhen-Yu Yin
zhenyu.yin@polyu.edu.hk
Hao Xiong
xionghao19529@gmail.com
Zhimin Zhang
zhangzhimin3210@163.com
Xiangsheng Chen
xschen@szu.edu.cn
Wanhuan Zhou
hannahzhou@um.edu.mo

² Key Laboratory of Coastal Urban Resilient Infrastructures (Shenzhen University), Ministry of Education, Shenzhen, Guangdong, China
³ College of Civil and Transportation Engineering, Shenzhen University, Shenzhen, Guangdong, China
⁴ Department of Civil and Environmental Engineering, The Hong Kong Polytechnic University, Hung Hom, Kowloon, Hong Kong, China
⁵ State Key Laboratory of Internet of Things for Smart City and Department of Civil and Environmental Engineering, University of Macau, Macau SAR, China

¹ State Key Laboratory of Intelligent Geotechnics and Tunnelling, Shenzhen University, Shenzhen, Guangdong, China

Suffusion can be induced when the coarser soil fraction fails to prevent the erosion of the fines subjected to a seepage flow. This complex phenomenon has also been extensively considered a common cause of heterogenization of the soil materials and deterioration of many structures [24, 71, 72]. The soil surface suffers scouring during rainfall as fine particles migrate within the coarse-grained skeleton. Local clogging in the pore space raises the pore water pressure and reduces the effective stress, which is the main cause of debris flows [17]. In shield tunnels, water ingress at the joints often accompanies suffusion of the soil, leading to structural damage [42]. Soil fluidization and subsequent erosion into defective sewer pipes lead to sinkhole formation. Continued development of sinkholes can even lead to ground collapse, causing huge economic losses and human casualties [48, 75]. In addition, decohesioned sandstones with weak consolidation are susceptible to being eroded driven by reservoir fluid during the oil recovery; thereafter, clogging up and instability of the well may be caused. Clogging of the eroded material also affects flow rate and stability [9]. The mechanism of suffusion has been investigated by amount of researchers through the conventional seepage experiments on natural soils due to its non-negligible consequence.

In the literature, the onset and evolution of suffusion are influenced by geometrical, hydraulic and stress conditions (i.e., a series of factors such as grain size distribution (GSD), particle type, hydraulic gradient as well as stress state). Kenney and Lau [26] presented a method for assessing the potential for grading instability based on GSD of the granular material and indicated that the erosion of loose particles within the porous network following seepage is influenced by GSD of the whole material. The suffusion-prone soils are described as internally unstable, and the shape of GSD appears as a key parameter in the degree of soil internal instability [53]. Chang [3] carried out a series of field jet index tests and pointed out that the main influential factors of soil erodibility are found to be GSD, fine content (FC), void ratio and plasticity index. Soils with relatively high fine fraction are susceptible to erosion under a low hydraulic gradient, and fine particle loss increases with the imposed hydraulic gradient [25]. Erosion tests were conducted on granular material and concluded that the hydraulic condition plays a central role in the initiation and continuation of suffusion [43, 46]. When the stress state approximates failure, the critical hydraulic gradient under compression stress conditions tends to increase and then diminish with the shear stress ratio [4]. In addition,

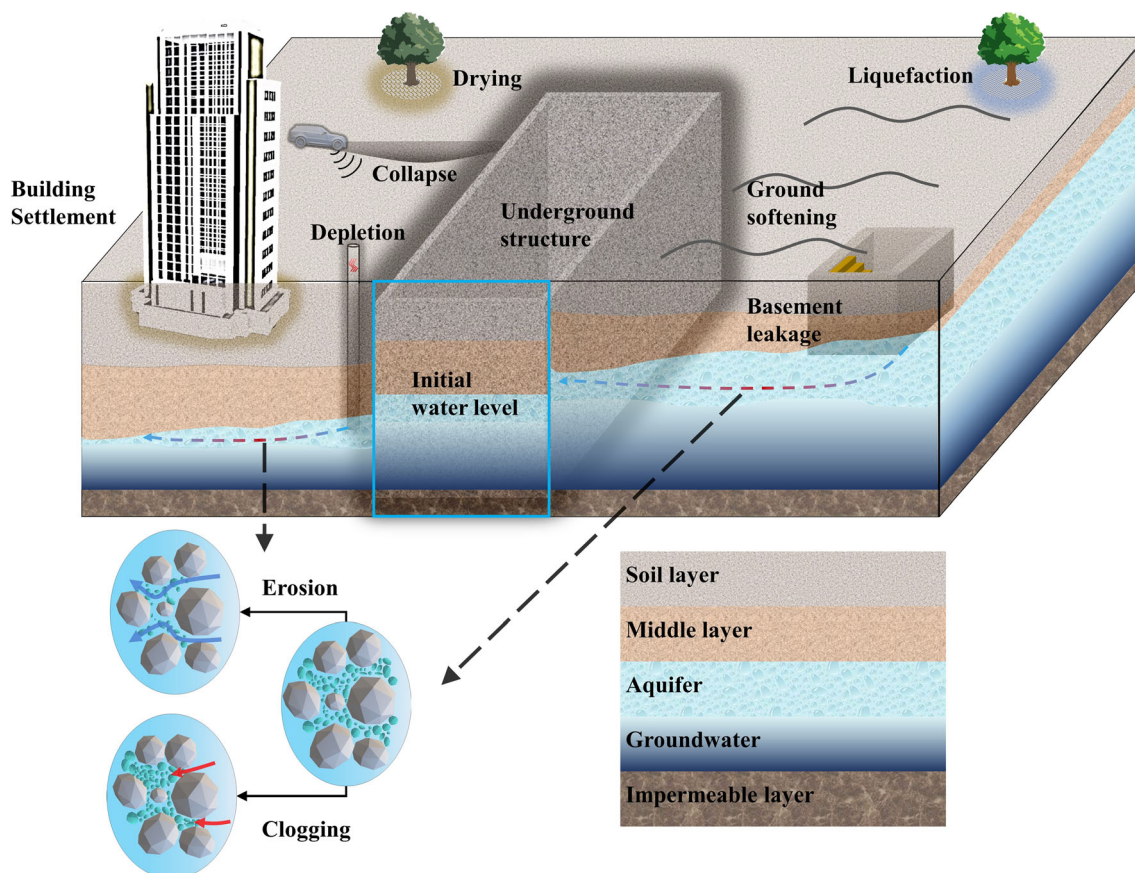


Fig. 1 Schematic diagram of suffusion caused by changes in groundwater seepage conditions

several studies have shown that the shape parameters of granular material are important factors affecting the resistance to suffusion [34, 47].

According to previous studies, the self-filtering and clogging frequently occur when continuous suffusion: the transmitted fines may be filtered or re-settled in the porous skeleton assembled by coarse particles [5, 61]. As a natural porous medium, the re-settlement of migratory particles within the soil skeleton during suffusion is a typical physical clogging phenomenon. The size ratio of constriction to particle and interaction forces could significantly affect the evolution of non-flowable zones [32]. Detached fines of approximate size to the pores are more likely to be intercepted, inducing the development of non-flowable zones [15]. Moreover, clogging efficiency is influenced by flow velocity and concentration of fines, and minor differences in particle size ratio affect both clogging rate and distribution [7, 10, 76].

Depending on the position of the clogged particle clusters, the clogging type can be classified as superficial clogging, internal clogging and mixed clogging, where the superficial clogging may be the main situation of clogging [10]. The appropriate fluid pore velocity is needed at all layers in soils for the steady transport of the detached fine particles during the progression of suffusion. Once transmitted fines are intercepted (transmission effect is prevented), local clogging occurs, and the local permeability subsequently decreases even when the hydraulic gradient increases [44]. Local flow rate varies with the clogged pores, which promotes a wider cluster, and this spreading behavior is quite effective in reducing the hydraulic conductivity [29, 62]. The increase in water content and pore pressure undoubtedly raises the risk of geotechnical engineering disasters. Conventional seepage tests on real granular materials have been performed widely to study the macroscopic phenomena and mechanisms of the development of clogging zones. However, the differences in particle migration and water flow between superficial and internal clogging are not negligible [10, 16].

In view of the limitation of the experimental study, grain-scale numerical modeling has provided a microscopic level understanding of a solid pathway to the results of macroscopic phenomena [39, 54, 58, 70, 74], where the discrete element method (DEM) is capable of capturing the movement information of each particle effectively. However, the selective removal approach without accounting for the fluid phase fails to reappear the changes in internal water flow and pore space in microstructure arising from local clogging. Natural soils are composed of multiphase materials, where saturated soils consist of two phases: solid and fluid. In the analysis of geotechnical engineering, the fluid–solid interaction should be necessarily considered to

investigate the mechanical properties of soils under undrained condition. In recent years, introducing fluid phase into the modeling has been extensively performed to detect the coupling information at the micromechanics scale [55, 60, 63]. Currently, numerical experiments of suffusion evolution were popularly performed by the coupled computational fluid dynamics (CFD) and discrete element method technique. CFD-DEM, a typical Eulerian–Lagrangian method, allows considering both macro- and micro- properties of the two phases and conduct with high-efficiency parallel computation [67]. Hu et al. [21] adopted this method to explore the influential factors and macroscopic responses on kinetics of suffusion, such as GSD, initial FC and hydraulic conditions. A series of CFD-DEM coupling simulations with different quantities of migratory fines were carried out to study the granular transmission effect [6]. At present, there is a lack of suffusion comprehension regarding the microscopic characteristics of the fine particles clogging development under the seepage action. Furthermore, most of the grain-scale numerical models simplify the materials with spherical particles, which ignores the effect of particle shape.

Contrary to ideal spherical particles, soil particles in nature tend to have more complex geometrical characteristics, and packings composed of irregular particles reflect more realistic void topology [31, 57]. These differences affect both fluid–solid interaction and clogging evolution [37, 50, 77]. Three main shape parameters, including sphericity, roughness and angularity, characterize the realistic granular material from different scales [35, 52], as shown in Fig. 2. Maroof et al. [34] study the coupling influence of GSD and shape on erosion susceptibility. When particle shape analysis is performed in practical applications, quantitative analysis of shape characteristics at a single scale is difficult to achieve [8]. Zhao and O’Sullivan [77] performed a series of simulations using CFD-DEM modeling and indicated that the angularity enhances the fluid–particle interaction forces and the resistance of suffusion. Xiong et al. [64] visualized the coarse particles as polyhedral and observed the particle shape has a negative feedback on suffusion. Aspect ratio (AR), the ratio of particle width to height, has a non-negligible effect on the shape coefficient [33].

In light of the above review, a framework is developed for the numerical representation of the interactions between irregular particles and fluid via a two-way coupled CFD-iDEM algorithm. The columnar soils are consolidated based on the irregular discrete element. The micromechanical consequences of shape effect on granular clogging are then numerically investigated. The paper is organized as follows. Firstly, the methodology is presented. In the next section, the validation of the proposed method, the establishment of the granular soils and the suffusion

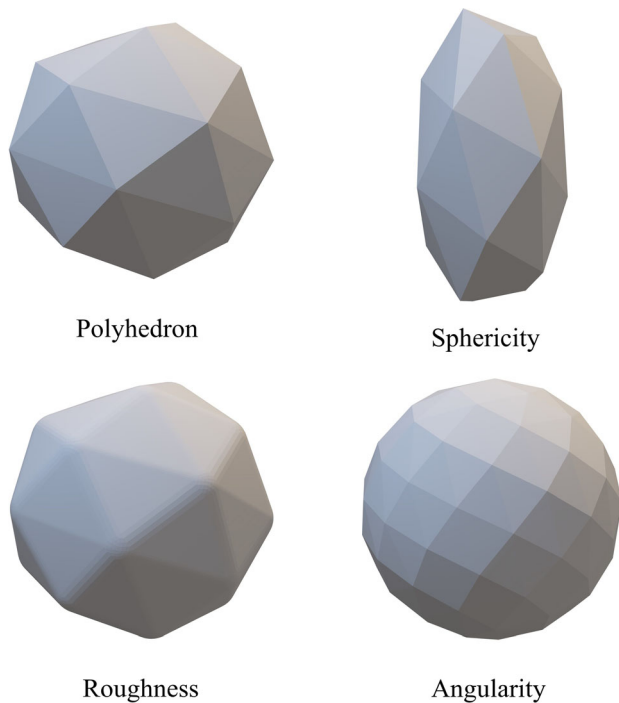


Fig. 2 Schematic illustration of shape parameters: sphericity, roughness and angularity

simulations are presented. Subsequently, numerical results summarizing the macroscopic responses and microscopic characteristics are discussed. Finally, the main conclusions of this study are summarized.

2 Description of the coupled CFD-iDEM method

The coupled CFD-DEM method has been widely used and validated by many previous researches [21, 65]. The two-way algorithm adopted in this study consists of three major parts: the CFD (fluid phase), iDEM (irregular particle phase) and the interaction information of fluid–particle system. The following is a detailed description of the governing equations for these three modules.

2.1 Fluid phase: CFD

The fluid domain is considered a continuum and governed using the locally averaged Navier–Stokes equations under transient conditions [27].

The mass conservation equation can be presented as:

$$\nabla \cdot (n\mathbf{u}_f) + \frac{\partial n}{\partial t} = 0 \quad (1)$$

where t is the time, n and \mathbf{u}_f account for the local porosity within an individual cell and the fluid velocity, respectively.

The momentum conservation equation is given by:

$$\frac{\partial (n\mathbf{u}_f)}{\partial t} + \nabla \cdot (n\mathbf{u}_f\mathbf{u}_f) = n\mathbf{g} - \frac{n\nabla p}{\rho_f} + \frac{\mathbf{F}_{p \rightarrow f}}{\rho_f} + \frac{\nabla \cdot (n\boldsymbol{\tau}_f)}{\rho_f} \quad (2)$$

where \mathbf{g} is the acceleration of gravity, ρ_f is the fluid density, and $\mathbf{F}_{p \rightarrow f}$ represents the interaction force exerting on the fluid imposed by the iDEM phase. p and $\boldsymbol{\tau}_f$ denote the locally averaged pressure and stress for the fluid.

2.2 Particle phase: iDEM and irregular particle

In the particle phase, the irregular particles are computationally solved by Newton's second law of motion and individually tracked following a Lagrangian method to capture the intergranular collisions and the trajectory of every single particle [27].

2.2.1 Irregular discrete element method

According to the translational and rotational motions of particle, the governing equations for particle i with mass $m_{p,i}$ and moment of inertia $\mathbf{I}_{p,i}$ are written as:

$$m_{p,i} \frac{d\mathbf{v}_{p,i}}{dt} = m_{p,i}\mathbf{g} + \sum \mathbf{F}_{c,i} + \mathbf{F}_{f \rightarrow p,i} \quad (3)$$

$$\mathbf{I}_{p,i} \frac{d\boldsymbol{\omega}_{p,i}}{dt} = \mathbf{M}_{f \rightarrow p,i} + \sum \mathbf{M}_{c,i} \quad (4)$$

where the $\mathbf{v}_{p,i}$ and $\boldsymbol{\omega}_{p,i}$ are the translational and angular velocity of the particle, respectively. $\sum \mathbf{F}_{c,i}$ and $\sum \mathbf{M}_{c,i}$ represent the total contact force and torque generated by the boundaries and other particles. $\mathbf{F}_{f \rightarrow p,i}$ and $\mathbf{M}_{f \rightarrow p,i}$ are the interaction force and torque induced by the fluid in the fluid–particle system, respectively.

The interparticle forces of irregular granular samples are calculated by adopting the Hertz–Mindlin contact force model, which is generally used to capture critical properties of granular material [64, 65]. The following equation can be used to calculate the normal component of the contact force F_n (the Hertzian spring-dashpot model) [19, 51]:

$$F_n = \hat{K}_H s_n^{\frac{3}{2}} + \hat{C}_H s_n^{\frac{1}{2}} \dot{s}_n \quad (5)$$

where s_n is the contact normal overlap, the stiffness coefficient \hat{K}_H and damping coefficient \hat{C}_H are described as follows:

$$\hat{K}_H = \frac{4}{3} E^* \sqrt{R^*} \quad (6)$$

$$\hat{C}_H = \sqrt{5} \eta \sqrt{m^* \hat{K}_H} \quad (7)$$

in which η accounts for the damping ratio, R^* and m^* are the equivalent radius and mass, respectively. E^* is the reduced Young's modulus, and the following expressions are used to describe these parameters:

$$\frac{1}{E^*} = \frac{1 - \nu_{p,i}^2}{E_{p,i}} + \frac{1 - \nu_{p,j}^2}{E_{p,j}} \quad (8)$$

$$m_{p,ij}^* = \frac{m_{p,i} m_{p,j}}{m_{p,i} + m_{p,j}} \quad (9)$$

$$R_{p,ij}^* = \frac{L_{p,i} L_{p,j}}{2(L_{p,i} + L_{p,j})} \quad (10)$$

where $\nu_{p,i}$ is the Poisson's ratio, and $E_{p,i}$ and $L_{p,i}$ are the Young's moduli and equivalent sphere diameter, respectively.

The Mindlin–Deresiewicz model is used in this study to calculate the tangential contact force F_τ described as:

$$\mathbf{F}_\tau = \eta_\tau \dot{s}_\tau \zeta^{\frac{1}{4}} \sqrt{\frac{6\mu F_n m^*}{s_{\tau,\max}}} - \mu F_n \frac{\mathbf{s}_\tau}{|\mathbf{s}_\tau|} \left(1 - \zeta^{\frac{3}{2}}\right) \quad (11)$$

$$\zeta = 1 - \frac{\min(s_{\tau,\max}, |\mathbf{s}_\tau|)}{s_{\tau,\max}} \quad (12)$$

where μ is the friction coefficient (including the static and the dynamic friction coefficients), and \mathbf{s}_τ and $\dot{\mathbf{s}}_\tau$ are the tangential relative displacement and velocity at the contact, respectively.

The tangential damping ratio η_τ can be written as:

$$\eta_\tau = -\frac{\ln \varepsilon}{\sqrt{\pi^2 + \ln^2 \varepsilon}} \quad (13)$$

where ε is the coefficient of restitution.

The maximum relative tangential displacement $s_{\tau,\max}$ can be given by:

$$s_{\tau,\max} = \mu s_n \left(\frac{1 - \nu_{p,i}}{2 - \nu_{p,i}} + \frac{1 - \nu_{p,j}}{2 - \nu_{p,j}} \right)^{-1} \quad (14)$$

2.2.2 Irregular particle

The polyhedral particle is adopted as the irregular discrete element in this study to investigate the shape effect. Based on the setting diameter of a sphere with an equivalent volume to the form being measured, the polyhedral particle size is calculated. The size of the smallest square channel the particle can pass through is referred to as the polyhedral particle size (Fig. 3a). The process to obtain the size of the smallest square channel goes through three steps: the determination of principal axis, slices and the largest distance. Firstly, all pairs of vertices on the particle are considered, where the pair of vertices farthest apart are regarded as the two endpoints of the principal axis (Fig. 3b). Then, the slice pair perpendicular to the principal axis is determined at two endpoints on any one edge of the polyhedral particle, which serves as the slice candidates for the smallest square channel (Fig. 3c). Subsequently, all vertices contained between the two limiting planes are projected orthogonally onto one of the planes. The projection point with the farthest distance from the edge endpoint is found, and this distance is the alternative size (Fig. 3d). Finally, the polyhedral particle size is determined as the maximum value among all size candidates.

The iDEM solves the motion equations for each particle during the suffusion process, updating its orientation and position represented with the global reference system. The vector-rotation pattern is used to present the orientation of an irregular particle. The orientation of an irregular particle with this representation is defined by the orientation of an attached local reference system, which rotates an angle θ about the axis determined by a unit vector, as depicted in Fig. 4a. Figure 4b illustrates the examples of the orientation of an irregular particle with respect to the vector-rotation pattern, and the rotation matrix R is given by [49]:

$$R = \begin{pmatrix} \cos \theta + u_x^2(1 - \cos \theta) & u_x u_y(1 - \cos \theta) - u_z \sin \theta & u_x u_z(1 - \cos \theta) + u_y \sin \theta \\ u_y u_x(1 - \cos \theta) + u_z \sin \theta & \cos \theta + u_y^2(1 - \cos \theta) & u_y u_z(1 - \cos \theta) - u_x \sin \theta \\ u_z u_x(1 - \cos \theta) - u_y \sin \theta & u_z u_y(1 - \cos \theta) + u_x \sin \theta & \cos \theta + u_z^2(1 - \cos \theta) \end{pmatrix} \quad (15)$$

The detection procedure is split into two separate phases (i.e., the determination of related particles and exact distance) to optimize the large computational process of contact detection due to the intricacy of the shape. The flowchart is depicted in Fig. 5a. As a first step, the related particles are defined as all other particles situated at a distance less than a predetermined distance (Fig. 5b),

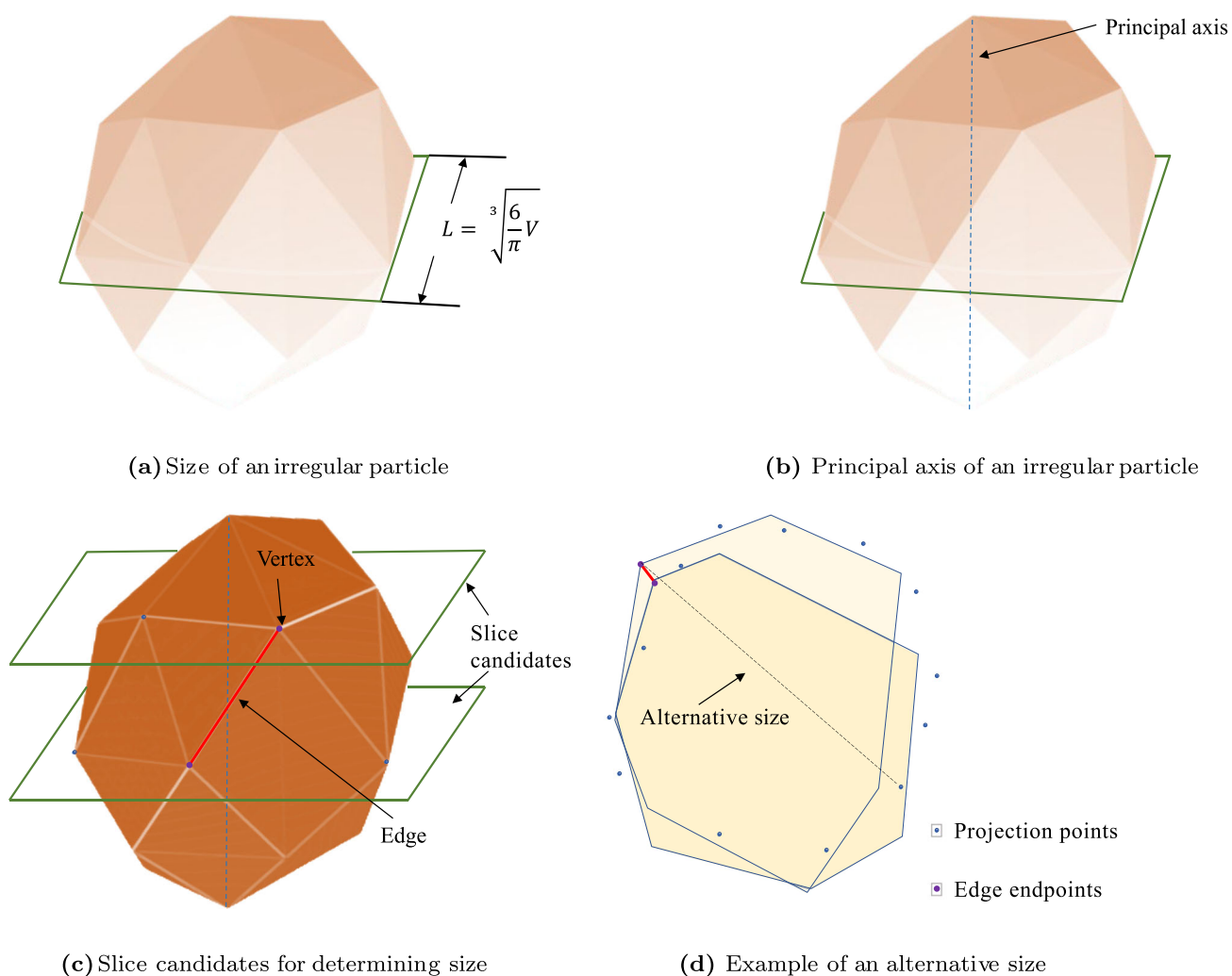


Fig. 3 Schematic diagram for determining size of an irregular particle

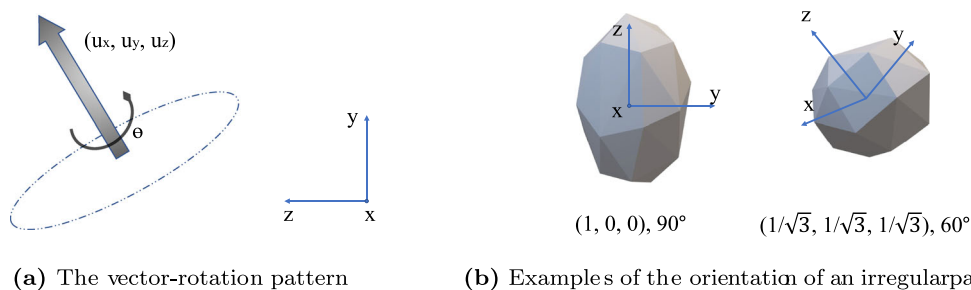
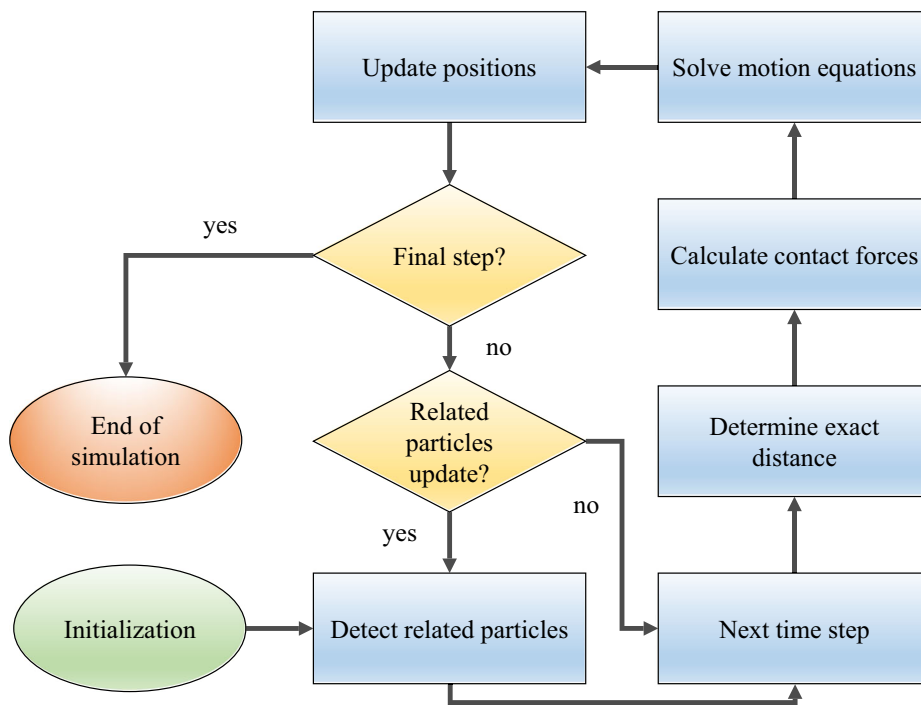


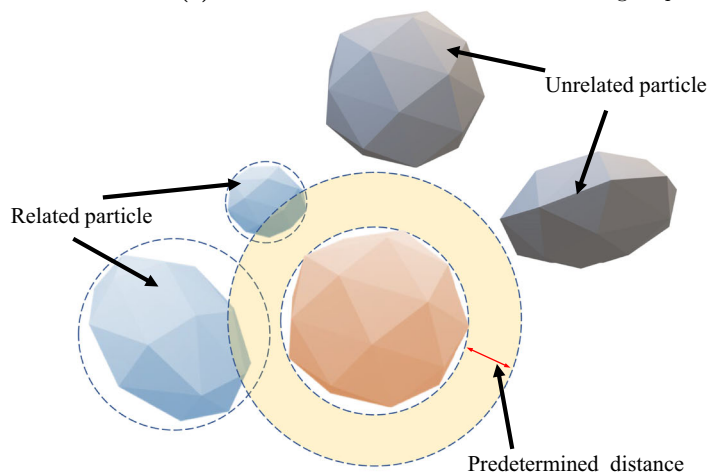
Fig. 4 Particle orientation of an irregular particle

which are considered the candidate contact particles. Consequently, the maximum distance that any pair of unrelated particles can move relative to each other is the predetermined distance. This operation involves every pair of particles, leading to a huge amount of computation, which is why this is only performed in partial timesteps. However, the candidate contact particles of all particles must be updated in time to prevent missing collisions. In

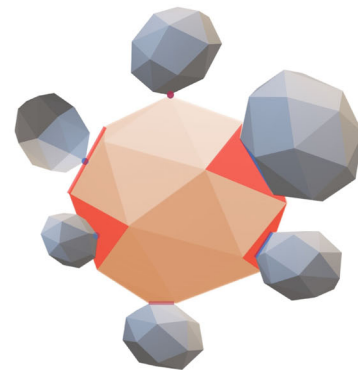
addition, this operation temporarily replaces the actual shape of a particle with a boundary sphere to optimize the detection of related particles. Next, using the most recent coordinates of the particles in the simulation, all pertinent geometrical information for each related pair of particle–boundary or particle–particle is calculated. It is worth noting that the candidate contact particles need to be updated frequently when the predetermined distance is



(a) Flowchart of contact detection between irregular particles



(b) Schematic diagram of related particles detection



(c) Different scenarios of interparticle contact

Fig. 5 Process of collecting contact information

small. On the contrary, too many particles need to be solved in the second stage when the distance is relatively large. The predetermined distance is given as 0.001m to balance efficiency and accuracy. Additionally, the second stage takes into account the actual irregular shape. The occurrence of interparticle contact is considered in various situations for the irregular particles and can be divided into the following types: vertex–vertex, vertex–edge, vertex–face, edge–edge, edge–face and face–face, as illustrated in Fig. 5c.

2.3 Interaction information of fluid–particle system

The fluid–particle system involves multiple forms of interaction forces [28], and drag force \mathbf{F}_D and pressure gradient force $\mathbf{F}_{\nabla p}$ are focused on in this study due to the modest translational and rotational motion of irregular particles during simulation. Therefore, the fluid–particle interaction forces can be written as:

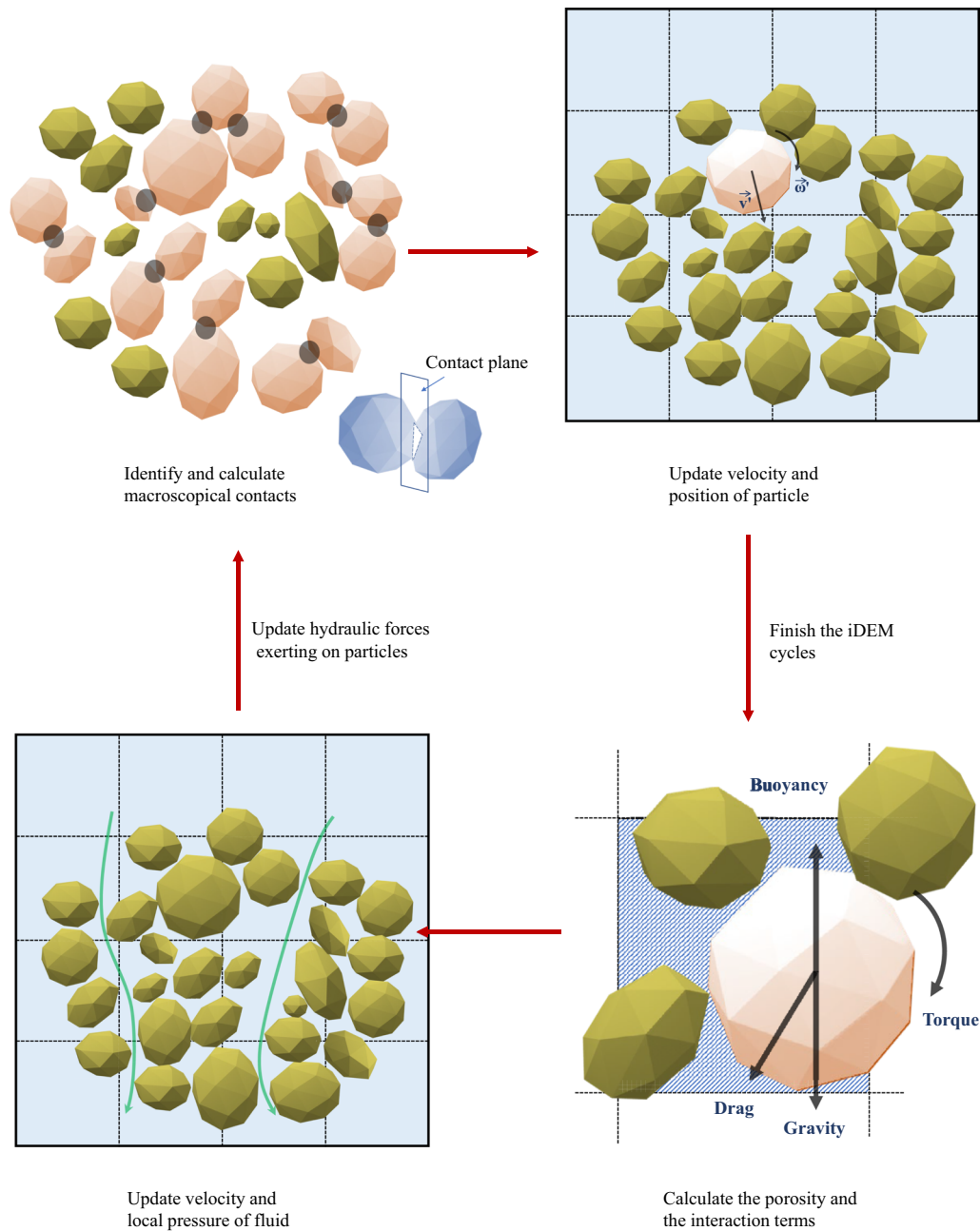


Fig. 6 Flowchart of the coupling procedure and data exchange between CFD and iDEM solvers

$$\mathbf{F}_{f \rightarrow p} = \mathbf{F}_D + \mathbf{F}_{\nabla p} \quad (16)$$

The equation of the calculation of the drag force \mathbf{F}_D on irregular particle is given by:

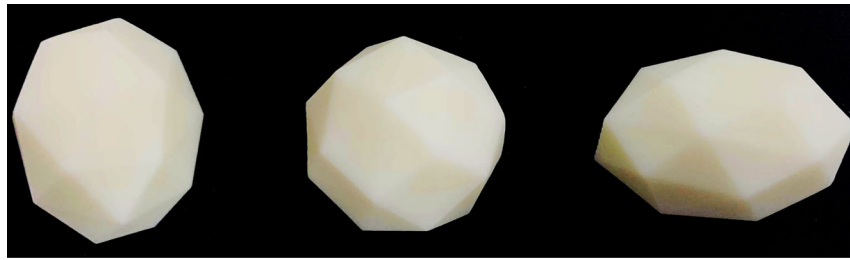
$$\mathbf{F}_D = \frac{1}{2} A' C_D \rho_f (\mathbf{u}_f - \mathbf{v}_{p,i}) \mid \mathbf{u}_f - \mathbf{v}_{p,i} \mid \quad (17)$$

where C_D is the drag coefficient, A' is the projected area of irregular particle in the flow direction. $\mathbf{u}_f - \mathbf{v}_{p,i}$ represents the relative velocity. It is worth noting that lots of C_D have been proposed. The Huilin and Gidaspow model has

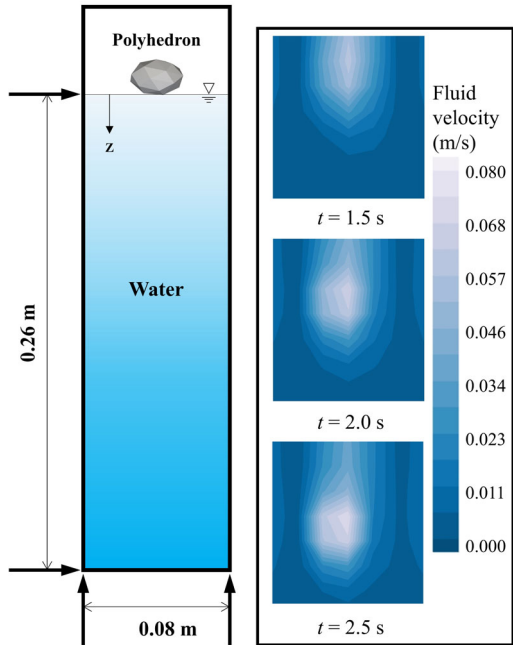
proved to be suitable for the study of suffusion, which effectively optimizes the transition between the Ergun relation and the Wen and Yu model [23]. That is:

$$C_{D_{Huilin\&Gidaspow}} = \psi C_{D_{Ergun}} + (1 - \psi) C_{D_{Wen\&Yu}} \quad (18)$$

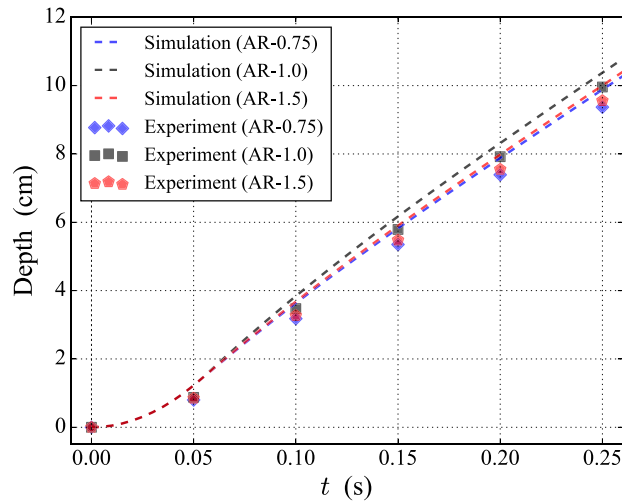
where the parameter ψ based on fluid volume fraction α_f is expressed by:



(a) The 3D printed polyhedral particles: AR-0.75, AR-1.0 and AR-1.5



(b) Schematic diagrams of apparatus and local velocity field during test



(c) Results comparison of the water-entry depth

Fig. 7 Water-entry test of a single irregular particle

Table 1 Material parameters used for the method calibration

Property	Value	Unit
<i>Water</i>		
Density	1000	kg m ⁻³
Viscosity	0.001	Pa s
<i>Particle</i>		
Density	1155	kg m ⁻³
Young's modulus	0.1	GPa
Poisson's ratio	0.3	–

$$\psi = 0.5 + \frac{1}{\pi} \arctan [150 \times 1.75 (0.8 - \alpha_f)] \quad (19)$$

The equation of the calculation of pressure gradient force $\mathbf{F}_{\nabla p}$ is expressed by:

$$\mathbf{F}_{\nabla p} = -V_p \nabla p \quad (20)$$

where V_p and ∇p account for the volume of corresponding particle and local pressure gradient, respectively.

2.4 CFD-iDEM coupling scheme

In this study, the coupled CFD-iDEM method based on the Eulerian–Lagrangian framework provides an effective way for the two-way exchange between the solvers of fluid–particle system, as indicated in Fig. 6.

At the beginning of the algorithm, the components of two phases and coupling model are initialized. Subsequently, the contact forces are first determined in the iDEM solver. The contact of the irregular particles is determined by the contact plane when they overlap each other. Next, new positions and velocities of particles are calculated by the equations of motion. The particle information is transferred to the fluid domain to calculate the local porosity and interaction terms. The information, both interaction and fluid mesh, will be updated after the

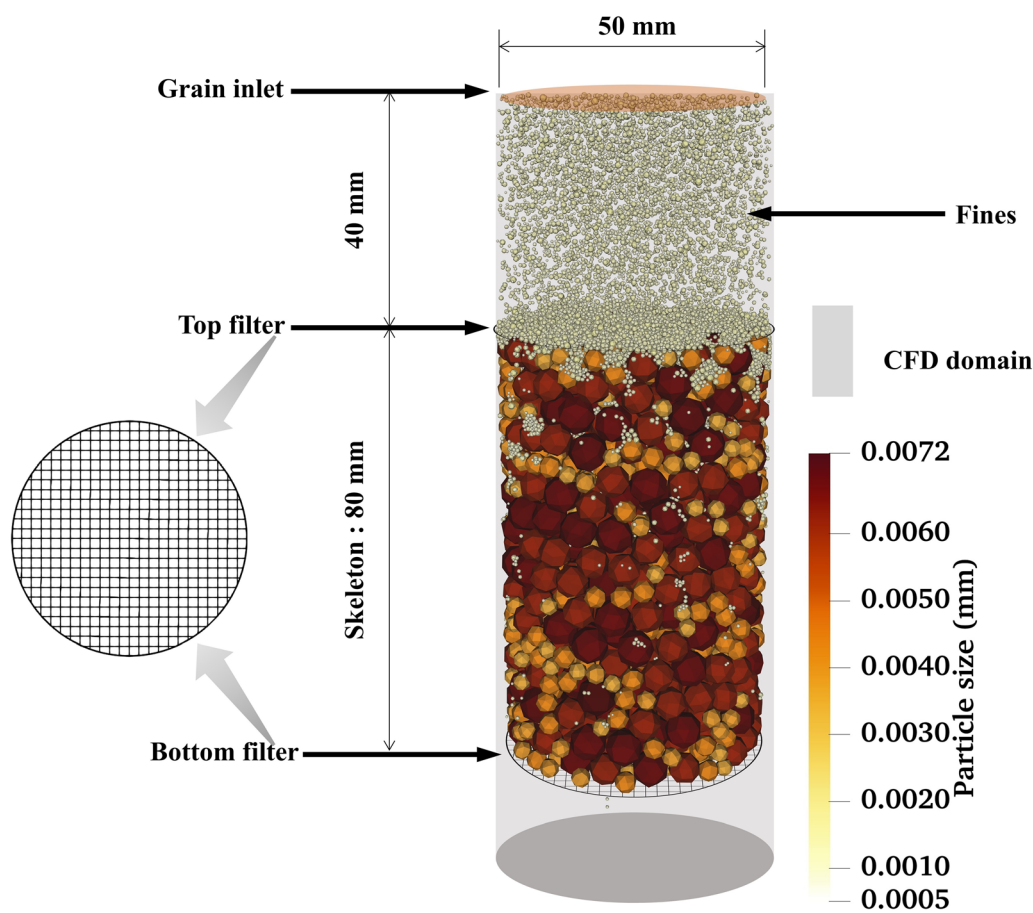


Fig. 8 The numerical model of suffusion based on the CFD-iDEM method

iteration has converged, which is transferred back to the iDEM solver. Operation of the loop is conducted to complete the entire calculation.

3 Method validation and model description

3.1 Validation of the CFD-iDEM method

Water-entry experiments of a single irregular particle are carried out to verify the proposed CFD-iDEM method. Three representative polyhedral particles (AR-0.75, AR-1.0 and AR-1.5) are generated and 3D printed, all with an equivalent diameter of 0.03 m, as shown in Fig. 7a. For the experiments, particle is released in tangency with the water surface. Dimensions of the cylindrical fluid domain are 0.08 m in diameter and 0.26 m in height, schematic diagrams of the experimental apparatus and local fluid velocity field during the simulation are presented in Fig. 7b. For the numerical simulations, parametric setups of the irregular particles are consistent with the experiments (including shape, size, density and initial











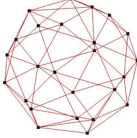


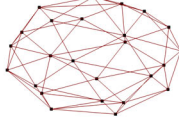



orientation). The detailed parameters of the water and particles used in the numerical simulation are illustrated in Table 1.

The evolution of the water-entry depth of the single polyhedral particle with the time is obtained and compared in Fig. 7c. The water-entry processes of the experiments show a slight delay, which might be related to the air cavity formed in the wake of a particle falling through the water surface. Both experimental and simulation results present the effect of particle shape on the interactions of the fluid–polyhedral particle with a good overall correlation. Hence, the proposed CFD-iDEM method is used here for the further study of suffusion.

3.2 Description of numerical simulation

Shape effects on clogging evolution mechanism of suffusion are investigated in the numerical model. The graphic description of granular samples and boundary conditions is presented in Fig. 8, of which the simulation domain is a cylinder.

Table 2 Details of different shapes

Shape	$y - z$ plane	$x - z$ plane	
Spherical particle (Benchmark case)			
Polyhedron ($N_{corners}=25$)			
Oblate polyhedron (AR-0.5)			
Oblate polyhedron (AR-0.75)			
Quasi-spherical polyhedron (AR-1.0)			
Prolate polyhedron (AR-1.5)			
Prolate polyhedron (AR-2.0)			

3.2.1 Model setup

For the particle domain, the irregular granular samples presented in this paper are composed of polyhedron particles with AR values ranging from 0.5 to 2.0. Additionally, the case in which the particle shape adopted sphere is simulated as benchmark. Detailed information about the particle shape is illustrated in Table 2, which covers sphere (benchmark case), quasi-spherical polyhedron (AR-1.0), oblate polyhedron (AR-0.5 and AR-0.75) and prolate polyhedron (AR-1.5 and AR-2.0). There are two groups of particles in the iDEM part of simulations, i.e., inflow fines (ranging from 0.5 to 1.3 mm) and coarse particles (ranging

from 3.3 to 7.2 mm). Figure 9 depicts the particle size distributions of the inflow fines and coarse-grained skeleton. It is worth noting that the difference between fine and coarse particles in one simulation is only the diameter of particle, there is no change in shape. Numerical models are developed to simulate the fine particles flow through the coarse-grained skeletons under seepage. The height of a coarse-grained skeleton is stabilized at 80 mm after consolidation within the impermeable wall of 50 mm diameter to reduce the boundary effect during simulation, as shown in Fig. 8. For the sake of computational stability and efficiency, the grain inlet is positioned 40 mm above the surface of coarse-grained skeleton, which can continuously

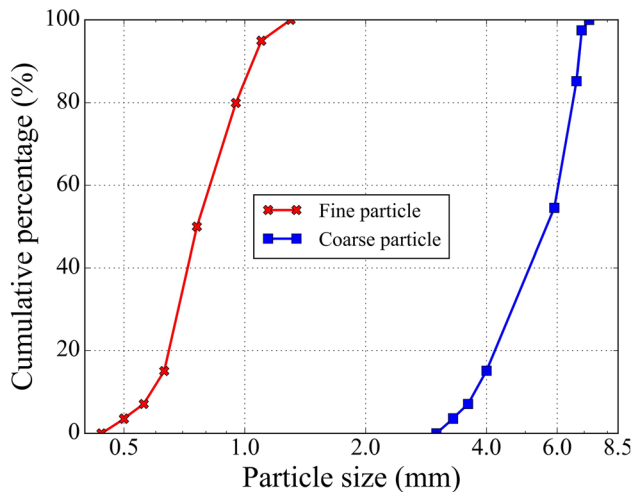


Fig. 9 GSDs of granular material in numerical simulations

Table 3 Material parameters used in the numerical simulation

Property	Value	Unit
<i>Fluid</i>		
Density	1000	kg m ⁻³
Viscosity	0.001	Pa s
<i>Particle</i>		
Density	2650	kg m ⁻³
Young's modulus	0.1	GPa
Tangential stiffness ratio	0.5	–
Poisson's ratio	0.3	–
Particle friction coefficient	0.2	–
Restitution coefficient	0.3	–

generate fine particles and set the boundary condition. The particle shape results in the difference of porous structure. In order to control the height of the sample, the number and quality of coarse particles are different, which also leads to such a difference in fines. Mass of fines is determined by setting the particle flow rate and time for continuous particle production in the grain inlet. In this study, the time for continuous particle production is set as 6 s, and the total mass of fines generated by the inlet is 5% of the corresponding coarse particles to guarantee the representativity of the simulated sample.

The fluid phase setting in the model is sufficiently large to adequately cover the particle area, of which the cylindrical rigid wall is assumed to have the impermeable and non-slip condition during suffusion. This setup is reasonable because the migration of particles is the main point. The top wall is the boundary of water inflow, and the bottom is set as outflow for the determination of downward

seepage direction. In this study, the boundary of water inflow is set as a constant inlet velocity, and the pressure and velocity at the outflow boundary are calculated by the CFD solver based on the incompressibility of fluid during suffusion. The fluid cell size is an important factor influencing the acquisition of fluid motion information. Too small size can lead to increased computational demands, potentially causing a decrease in simulation efficiency, while too large size fails to accurately capture the fluid movement [22, 56]. Therefore, the fluid cell size is given as 0.012 m. The standard $k - \varepsilon$ model is employed in the suffusion simulation of water flow. The parameters of the fluid cell are derived based on the behavior of pure water under the pressure of 100 kPa and the normal temperature [38].

It is worth noting that the processes of both the discrete element modeling and the suffusion do not consider gravity for the isotropic granular sample [56]. The total simulation time for suffusion is 12 s for each condition. The time steps for iDEM and CFD are 4×10^{-7} and 2×10^{-4} s, respectively. In all, Table 3 summarizes the parameters and arrangement regarding numerical simulation, which is a reference to previous studies and more in line with the natural soil particle [20, 21, 64]. The CFD-iDEM simulations are calculated on GPU device (NVIDIA GeForce RTX(TM) 2080Ti).

3.2.2 Simulation of suffusion

The simulation is operated into three stages: skeleton generation, consolidation and suffusion. Granular specimens are first established in iDEM solver before coupling with CFD. Coarse particles with the given GSD are first generated into the iDEM domain confined by a cylindrical rigid wall. The multi-layer consolidation method with an axial-directional compressive load of 100 kPa is conducted in order to ensure that the porous structure is as homogeneous as possible. The prepared coarse-grained skeletons are shown in Fig. 10. In addition, the initial porosity of each porous skeletons is 0.394, 0.367, 0.358, 0.381, 0.345 and 0.343 in order. The discrepancy is related to the orientation preference and sharp edges of polyhedral shapes [13, 14]. After the iDEM model is prepared, the velocity at the inlet patch of iDEM domain is activated, at which moment the simulation enters the CFD-iDEM coupling procedure. To simulate the flow, the water seeps at a velocity of 0.02 m s^{-1} , and the initial velocity of fine particles is consistent with it. During the first 1 s of the coupling process, the top and bottom plates of the coarse-grained skeleton are sealed for the saturated state of sample. In this period, the grain inlet for fines is not activated. Afterward, the two plates are replaced with rigid permeable

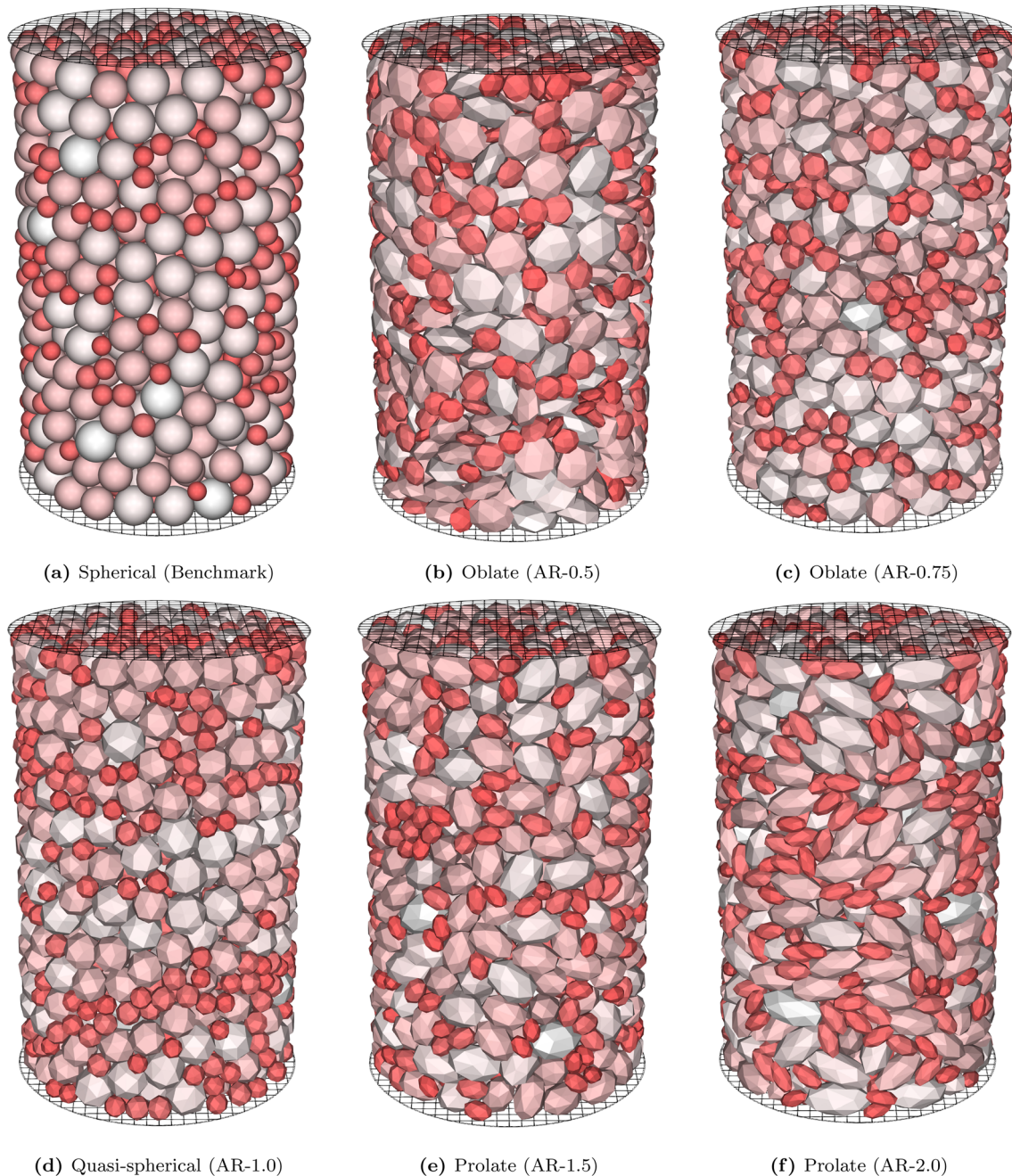


Fig. 10 Coarse-grained skeletons with different shapes: sphere and polyhedron (AR values ranging from 0.5 to 2.0)

filter, and the fine particles are generated. The sieve hole size of the rigid permeable filters is larger than the largest fine particles and smaller than the smallest coarse particles, as shown in Fig. 8. Such a pore opening filter allows the migration of fines, while coarse particles are confined within the skeleton area. Grain inlet for fines closes at 7 s. The migration and clogging of fine particles are then continued to be observed.

4 Results and discussion

4.1 Migration and clogging of fine particles

In the literature, there is a noteworthy difference in the distribution of the clogging delayed flow direction of fine particles in porous medium [10, 73]. The volume of clogging clusters decreases with the distance from the entrance [16]. Therefore, in combination with the microscopic analysis (which will be discussed in detail later), the

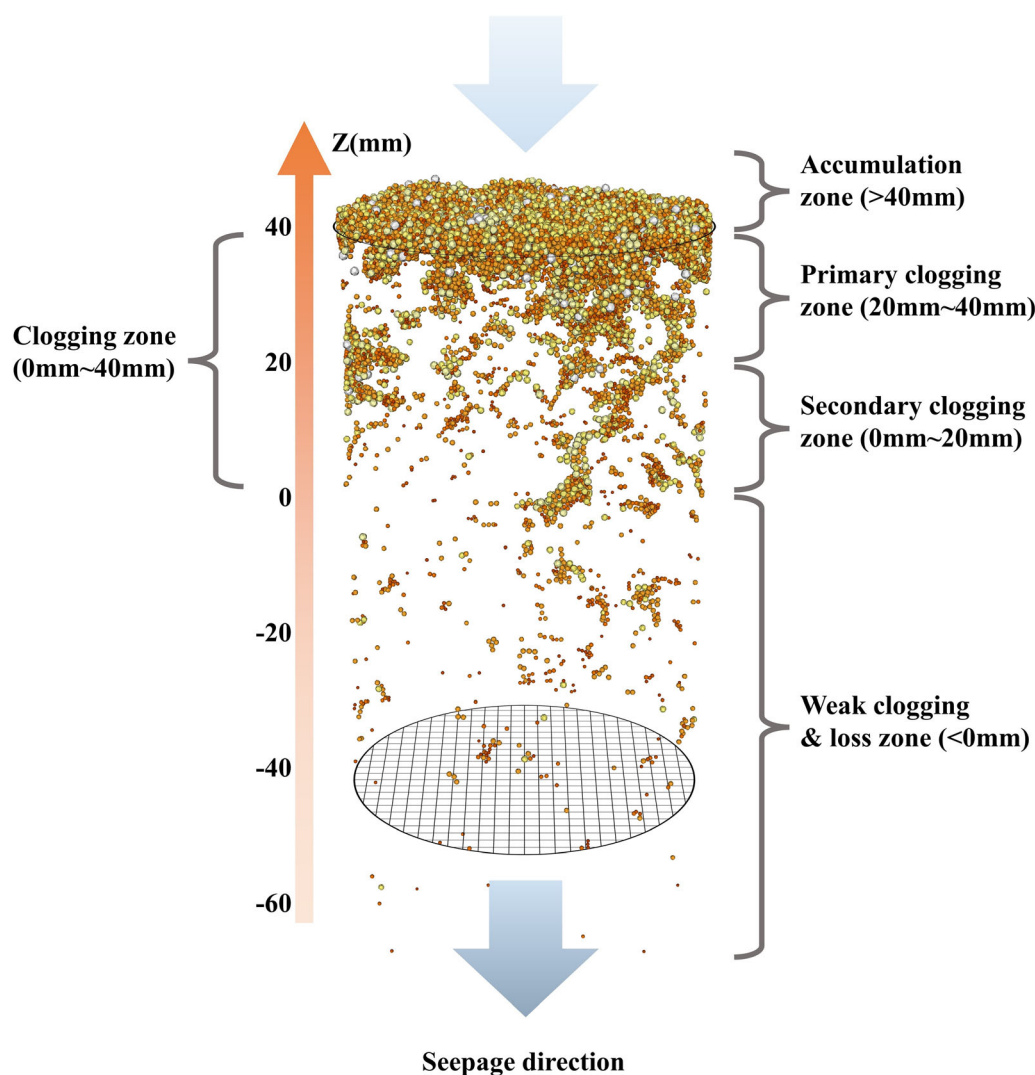


Fig. 11 Schematic illustration of vertical zoning

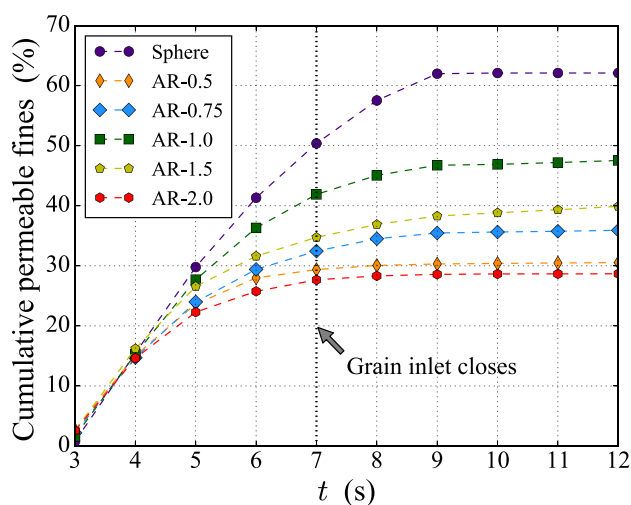


Fig. 12 Cumulative permeable fine particles with simulation time

entire seepage region is divided into the following zones according to the different locations of the fine particles, as shown in Fig. 11 (the display of coarse particles is hidden).

Figure 12 shows the cumulative permeable fine particles (i.e., the fine particles with longitudinal location below the top filter), which reflects the percentage of fine particles penetrating into the coarse-grained skeleton. From the simulation results, it is evident that the polyhedral shape has an influence on the migration of detached particles. The polyhedral shapes with different AR values constrain the transport of fine particles to various degrees, which promotes the accumulation of fines above the top filter. Irregular particles are more likely to clog, further forming particle bridging and arches [18]. Especially, the final values of permeable fines are 30.55% and 28.68% for the case with AR values of 0.5 and 2.0, which means that 69.45% and 71.32% of the fine particles are intercepted by the top filter and fail to enter the coarse-grained matrix. It

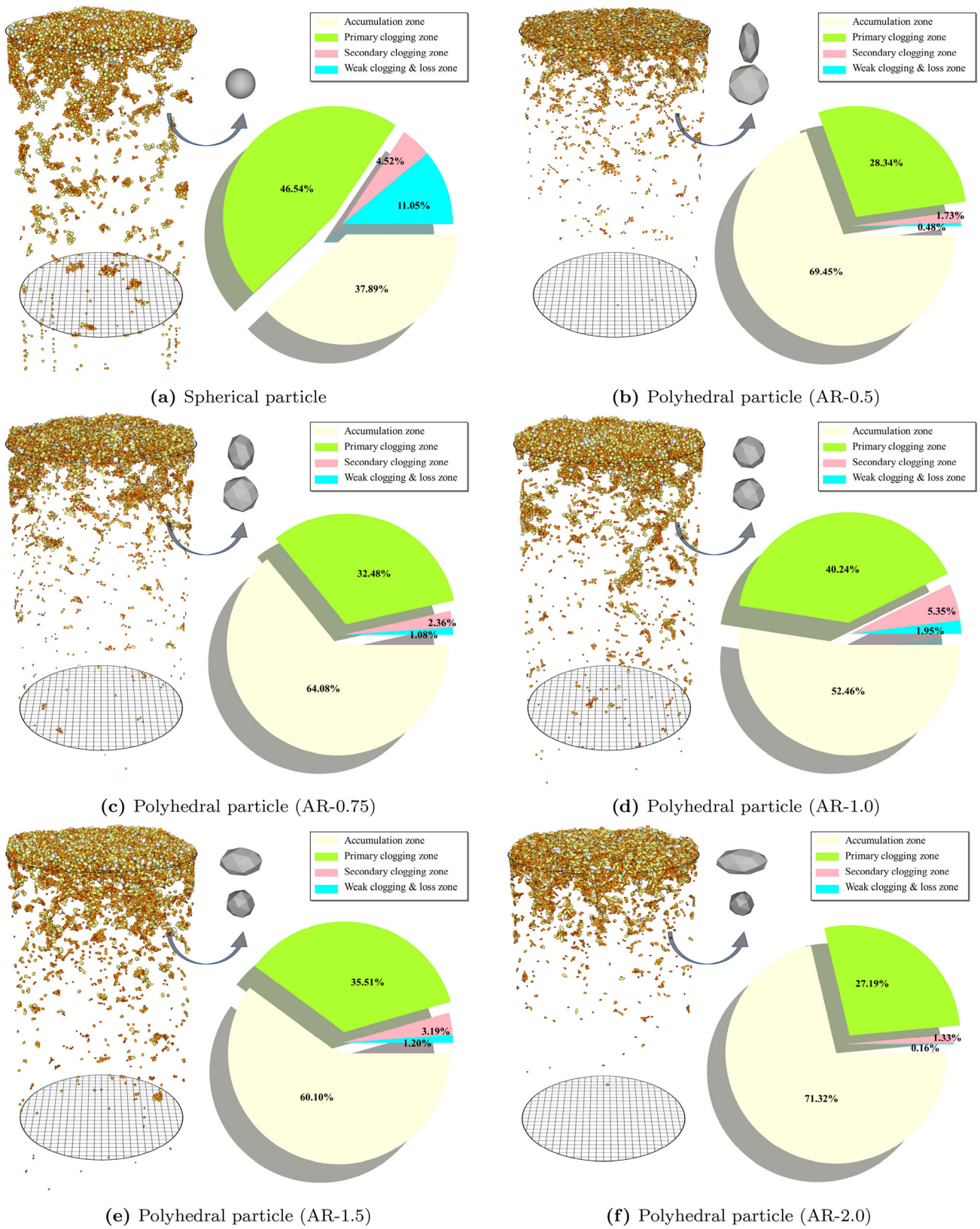


Fig. 13 Distribution of fine particles at the end of suffusion ($t = 12$ s)

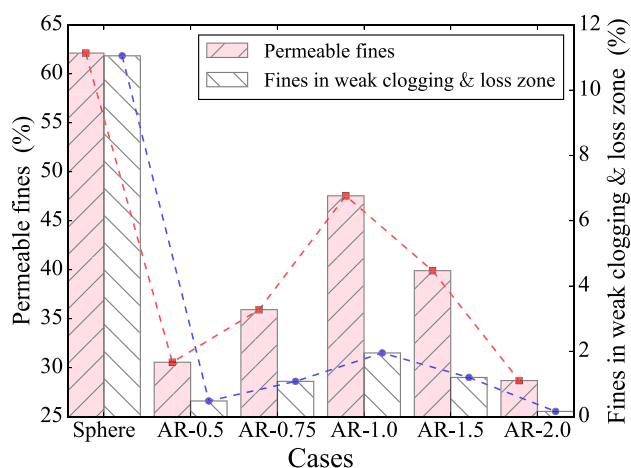


Fig. 14 Summary of final values for permeable fines and fines in weak clogging and loss zone

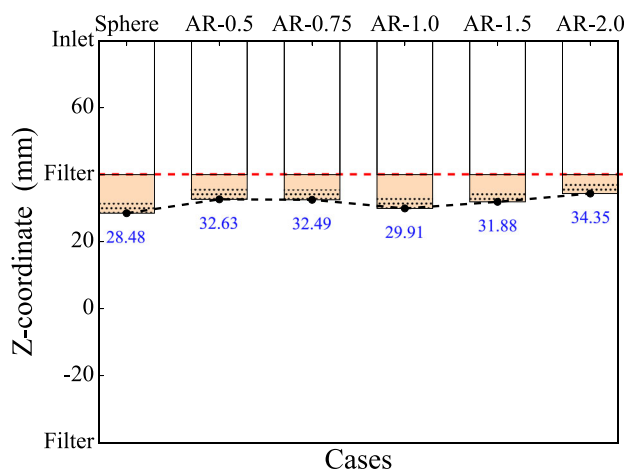


Fig. 15 Average z -coordinate of the fines remaining in the skeleton for all cases

can be observed that AR-1.0 with the shape closest to the sphere has the largest value of the cumulative permeable fine particles in the polyhedral cases (the AR value of spherical particles can be considered as 1.0). Xiong et al. [64] described similar evolutionary characteristics. Furthermore, oblate polyhedrons (AR-0.5 and AR-0.75) and prolate polyhedrons (AR-1.5 and AR-2.0) contribute more significantly to the accumulation of fines than quasi-spherical polyhedrons (AR-1.0). All cases reach an almost stable state when seepage ends, where cases with relatively low values of the cumulative permeable fines (AR-0.5 and AR-2.0) achieve the stable stage earlier (about 8 s). Broad clusters of fines accumulate earlier above the top filter, hindering the migration of subsequent fines.

The statistics of the distribution of fine particles at the end of suffusion ($t = 12$ s) are shown in Fig. 13. In addition, microscale distribution of fines is added to visualize the cluster information inside the skeleton. Gerber

et al. [16] concluded two different scenarios that may be encountered by migratory fines: caking (outside the filter) and depth filtration. As shown in Fig. 13b, f, more than half of the polyhedral fines accumulate outside the top filter, further forming caking. For the case with spherical particles, 37.89% of the fines failed to enter the coarse-grained skeleton, although it is observable that some of the exposed filter holes are not covered by the caking. Moreover, the content of fines in the primary clogging zone is the highest for all cases. According to the microscopic distribution, both the size and distribution of clogging clusters decrease gradually with the direction of seepage. As expected, there are 11.05% of spherical fines that can traverse the clogging zone, which far exceeds the fines content of polyhedral particles in the weak clogging and loss zone. Spherical case is more prone to migration than the soil sample with angular or low sphericity grains [34]. The highest content of fines in the weak clogging and loss zone is only 1.95% for all cases with polyhedral particles (Fig. 13). These results demonstrate the prone to clogging due to the interlock effect between polyhedral particles, contributing to the establishment of interparticle contacts that may resist torque and develop bridging [18]. Compared to the angle-free nature of spherical specimen, the angularity appears as a key parameter in enhancing the interparticle occlusion and interlock effect of polyhedrons [41, 78].

Figure 14 shows the values of the cumulative permeable fines (Fig. 12) and fines within weak clogging and loss zone after the suffusion simulations ($t = 12$ s), which depicts the similar shapes with cusps at AR value of 1.0. Specifically, for these two final values reflecting mobility, polyhedral specimens are much smaller than spherical cases. The higher the degree of deviation of polyhedral particles from the sphere, the smaller the values. Moreover, Fig. 15 depicts the average z -coordinate of the fines remaining in the matrix at the end of simulation ($t = 12$ s) along the seepage direction. A large number of fines in the primary clogging zone are captured by the pore space and form the non-flowable caking, preventing the penetration of subsequent particles. In addition, at the end of the simulation, 6.48% of the fine particles (Sphere) flow out of the bottom filter. In contrast, no outflow of fines was observed in the AR-2.0 case, the polyhedral fines in the weak clogging and loss zone are completely blocked in the skeleton. Results indicated that the main influence of particle shape on clogging under the seepage action is the clogging rate, with particles that deviate from a spherical shape being less susceptible to moving deeper. This can be related to the relatively larger mean pore length, decreasing the tortuosity [2].

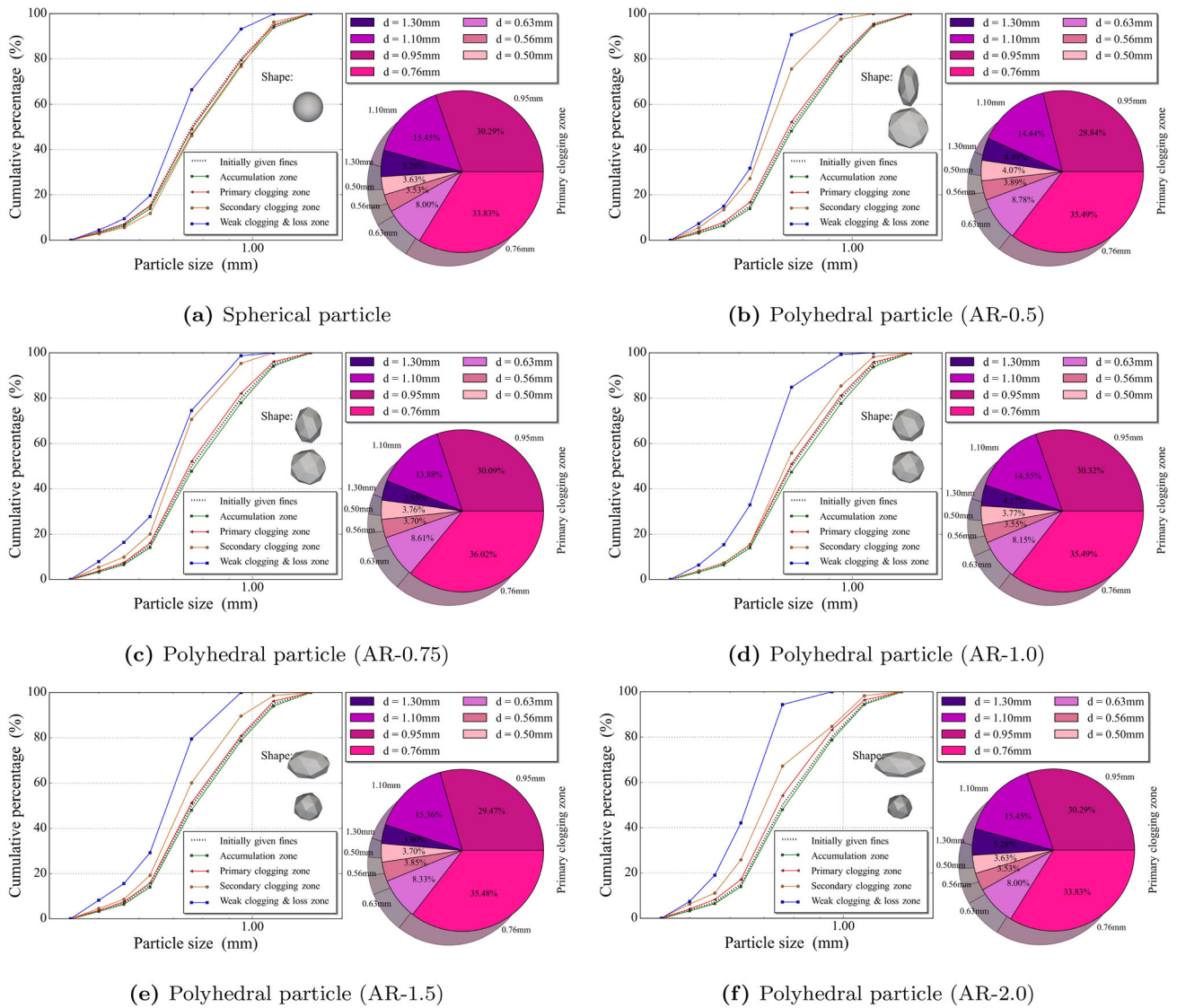


Fig. 16 Particle size distribution curves of different zones for all cases

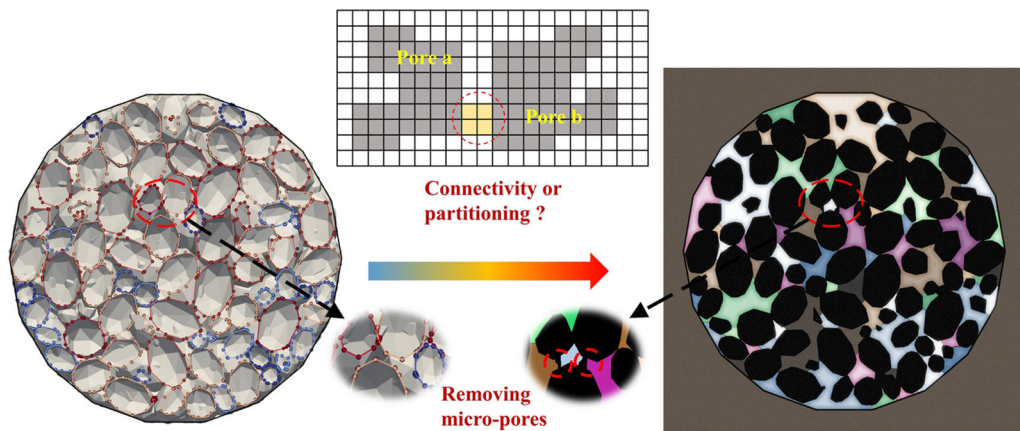


Fig. 17 Schematic drawing of the image processing techniques

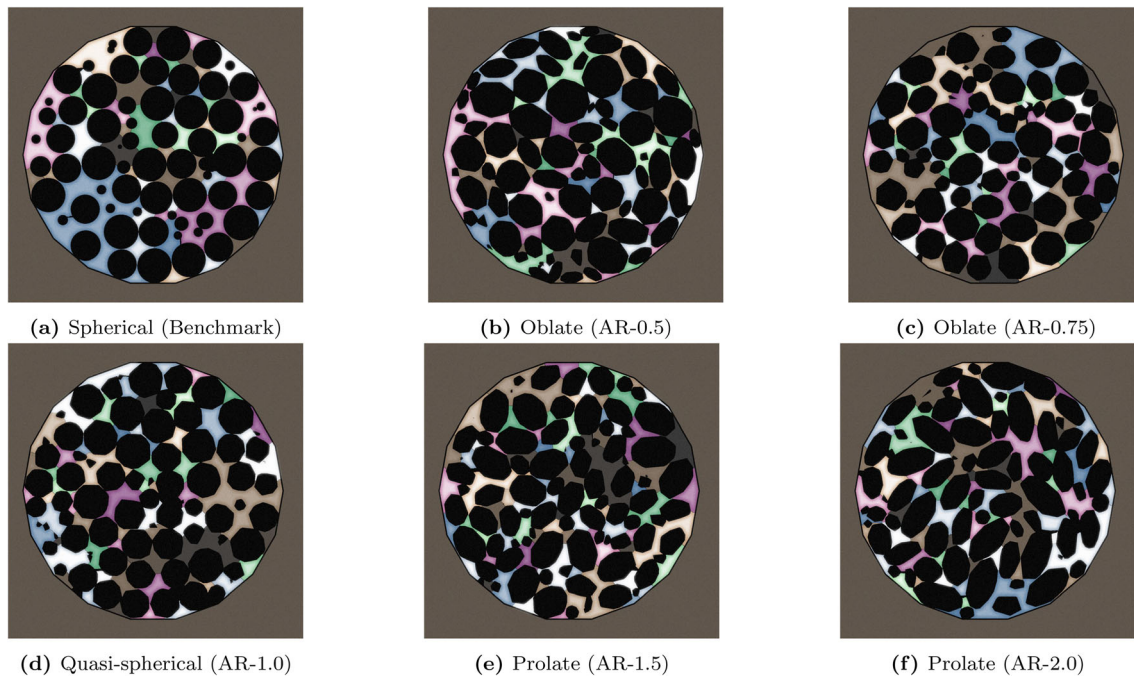


Fig. 18 Pore distributions in the cross sections of coarse-grained skeletons packed with different shapes at 35 mm

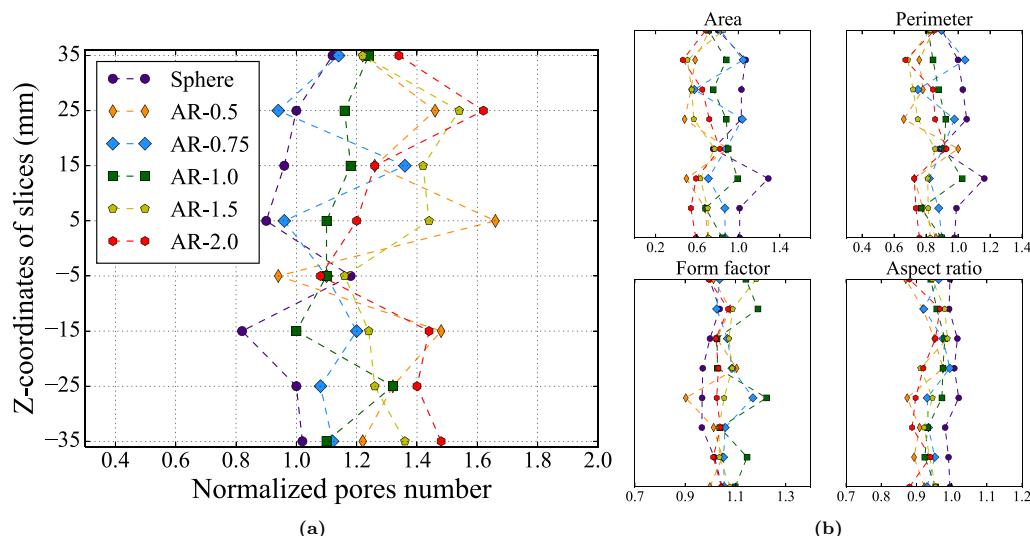


Fig. 19 Quantitative analysis of pore characteristics: number N_p , area A_p , perimeter P_p , form factor F_p and aspect ratio Ar_p

4.2 Grain size distribution of migratory and clogging fines

To investigate the effect of coarse-grained skeletons on the fines retention of different sizes under a given fluid condition, Fig. 16 shows the fines size distributions in different zones at the end of suffusion ($t = 12$ s). The distribution curve of each zone is compared to the initially given fines (Fig. 9) flowing from the grain inlet. In addition, the specific percentage of fines with different sizes in the primary clogging zone is plotted on the right side of the

distribution map. The GSD curves of the primary clogging zone and the initially given fines are almost identical for the spherical specimen (Fig. 16a), which shows the close clogging efficiency for spherical fines with different sizes. An interesting phenomenon is observed in the polyhedral specimens, where the initial fines curve is sandwiched between accumulation zone and primary clogging zone (Fig. 16b, f). Furthermore, all specimens exhibit a noteworthy deviation of GSD in the weak clogging and loss zone from the initial condition. Even for the spheres that are most prone to migration, only 0.22% of the largest fines

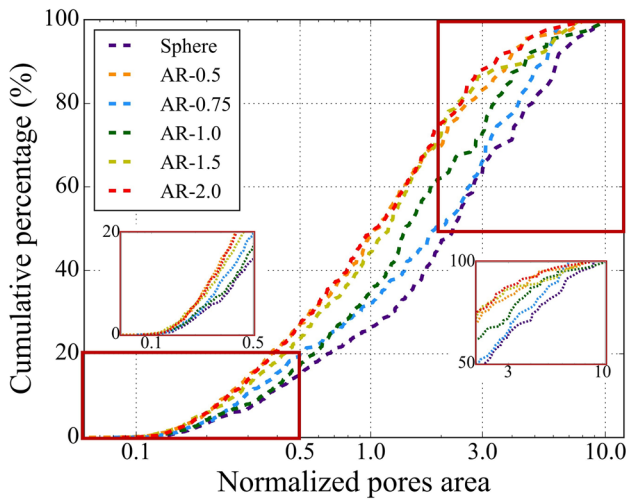


Fig. 20 Cumulative percentage of pore areas

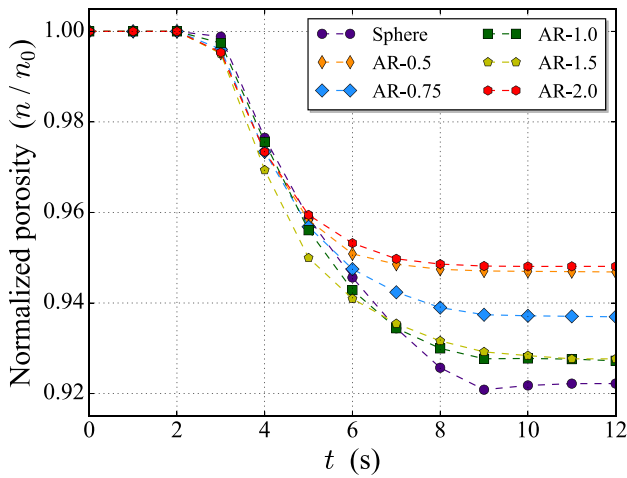


Fig. 21 Evolution of normalized porosity with simulation time

($d = 1.30$ mm) are in the GSD of weak clogging and loss zone. However, for all polyhedral cases, the largest fine particle is absent in the weak clogging and loss zone. In cases with AR values of 0.5, 1.5 and 2.0, specimens with a high degree of divergence from sphericity, even fine particles with a diameter of 1.10 mm were not observed. The results reveal that the transmitted particle with a large size is more prone to accumulate above the filter or within the clogging zone, failing to enter the skeleton or penetrate deeper.

4.3 Quantitative evaluation of connected pores and permeability

The pore structure of porous media significantly affects the clogging characteristics of particles, where the pore morphology of grained skeleton is affected significantly by both particle size and shape [13, 14]. The cross sections of

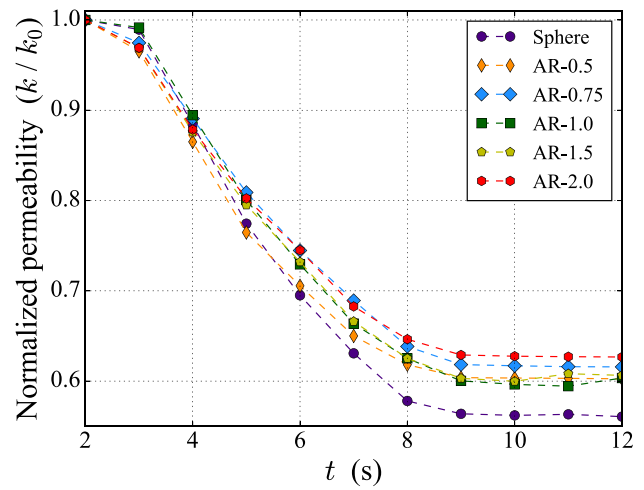


Fig. 22 Evolution of normalized permeability with simulation time

the consolidated packing of coarse particles are extracted and the pore characteristics are subsequently quantified by image processing techniques, as shown in Fig. 17. The process of obtaining pore morphology is summarized in the following steps: capturing particle boundaries, delineating regions of connected pores, filling the particle and pore phases, and removing micro-pores. The size of the smallest fine particle (0.5 mm) is adopted as the element size for determining the connectivity or partitioning between adjacent pores. The pore information of various cross sections (ranging from -35 to 35 mm) is quantified from the coarse-grained skeletons along the hydraulic direction, of which the pore distributions of the cross sections with a z -coordinate of 35 mm are illustrated in Fig. 18. The cross section of the skeleton with spherical particles visibly displays fewer and larger connected pores (Fig. 18a), which is responsible for its weak clogging property. Compared to the oblate and prolate cases, there exist similarly large connected pores between quasi-spherical

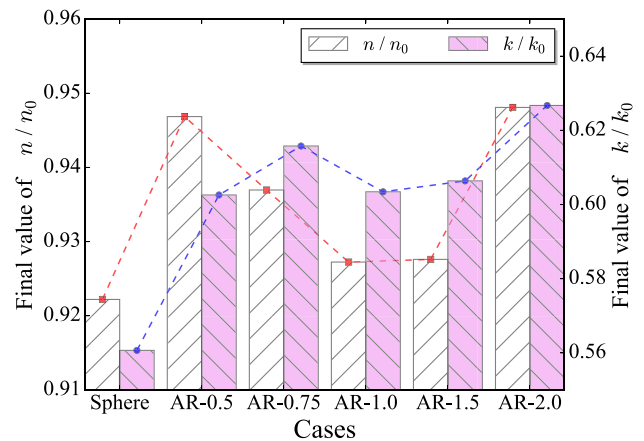


Fig. 23 Summary of final values for normalized porosity and permeability

polyhedrons (Fig. 18d). Additionally, the connected pores near the impermeable wall are more widely extended, and the preferential flow paths can lead to heterogeneous distribution of fines [36]. Figure 19 plots the longitudinal variation of the parameters characterizing the connected pores, with all statistics normalized by the average of the corresponding parameters in the spherical case. Fewer connected pores and less overall fluctuations in quantity in the spherical and quasi-spherical samples reflect larger connected pores and greater homogeneity, as shown in Fig. 19a. As the degree of deviation from the sphere increases, the fluctuation range widens, especially in the case with AR values of 0.5 and 2.0, which reflects the heterogeneity of the irregular particle orientation. Further, the longitudinal evolution of the normalized area A_p , perimeter P_p , form factor $F_p (= \frac{4\pi A_p}{P_p^2})$ and aspect ratio Ar_p is displayed in Fig. 19b, where Ar_p is determined as the ratio between the minimum Feret diameter and the maximum Feret diameter [45]. Spherical and quasi-spherical samples exhibit larger pore space and better connectivity internally. Moreover, the polyhedral skeletons show narrower and more complex pore boundaries. Figure 20 counts the cumulative percentage of all pore areas in the cross sections at eight different locations, with the area magnitude normalized by the mean of the spherical case. More small pores in irregular particle aggregates are due to the smaller throat size between the particle corners, which prevents the adjacent pores from fusing into a connected state. It is noteworthy that the connected pores in AR-1.5 appear relatively small, and a similar pattern was found by Gan et al. [14]. It has been illustrated that AR-1.5 in polyhedral cases is second only to quasi-spherical when counting cumulative permeable fines (Fig. 12).

Given the analysis above, the pore characteristics extracted from the cross sections present information on the morphology of the pores, the comparison with the permeation distribution of fines suggests that the process of particle migration is not purely determined by pore size and shape, but may also be influenced by differences in contact patterns and susceptibility to bridging due to particle shape. Microscopic analysis (force network and anisotropic characteristics) will be discussed subsequently.

Figure 21 shows how the normalized porosity evolves in the soil–fluid system, here only for the clogging zone to avoid excessive averaging. The results show that the evolution of porosity follows a similar pattern to the migration behavior. The polyhedral skeleton (AR-1.5) has significant pore variation due to the low initial porosity. In contrast, the polyhedral skeleton (AR-2.0) has a significant clogging efficiency, resulting in a low degree of porosity decrease,

which is also observed in the skeleton with high oblateness (AR-0.5).

Figure 22 depicts the variation of the local permeability of clogging zone with time, which plays a non-negligible characteristic reflecting the effect of clogging on the flowing nature of the coarse-grained skeleton during suffusion [1, 10]. The local permeability is calculated by Darcy's law:

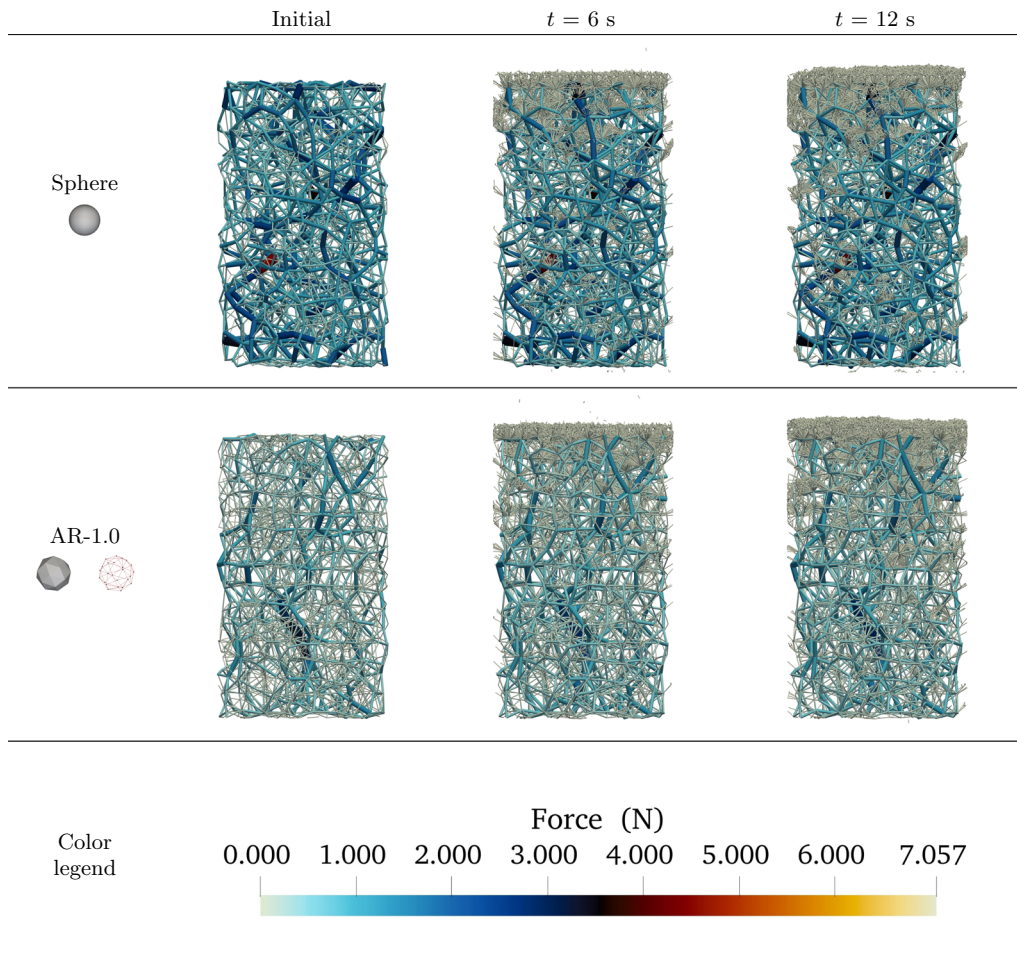
$$k = -\frac{u\gamma_w dZ}{dp} \quad (21)$$

where γ_w is the fluid volumic weight.

The result shows a significant reduction in local permeability for spherical specimen compared to polyhedrons. The higher initial porosity of spherical packing indicates that more space is available to capture the migratory fines. Also, the more substantial suffusion susceptibility allows more transmitted particles to traverse the top filter and thus be captured by pores in clogging zone (Fig. 12). The normalized porosity and local permeability considering different particle shapes at the end of suffusion are shown in Fig. 23. The effect of particle shape on skeleton porosity is similar to the distribution law of transmitted particles in this model (Fig. 14). The coarse particles forming the skeleton are highly stable after consolidation by a given axial-directional load. Therefore, the macroscopic reduction of pore space depends on the retention of fines. Changes in permeability are accompanied by transportation and clogging of fines [11]. The oblate polyhedron with AR = 0.5 has the largest cross-sectional area in the $y-z$ plane among all particles (Table 2), exerting the greatest influence on the distribution of pores on the cross section. The intense fluctuations of morphological indicators observed in Fig. 19 indicate that the local clogging of convoluted and discontinuous pores results in a more pronounced reduction in local permeability [68]. For permeability, in addition to a more substantial reduction in spherical specimens, the permeability of polyhedral packing with different AR values is also likely to depend on organized alignment, preferred orientation and the connectivity of pore space due to contact between polyhedrons [14, 41, 64, 69].

4.4 Evolution of force network

The clogging effect of migratory fines during the continuation of suffusion is not only reflected in the macroscopic features mentioned above but also reorganizes the soil properties at the microscopic level. In previous studies, it was found that normal contact force is much more critical than tangential contact force in the analysis of the deviator stress tensor [30, 78]. Table 4 shows the evolution of the force network for spherical and quasi-spherical cases,

Table 4 Evolution of force chain during suffusion for the cases with spherical and quasi-spherical particle (AR-1.0), respectively

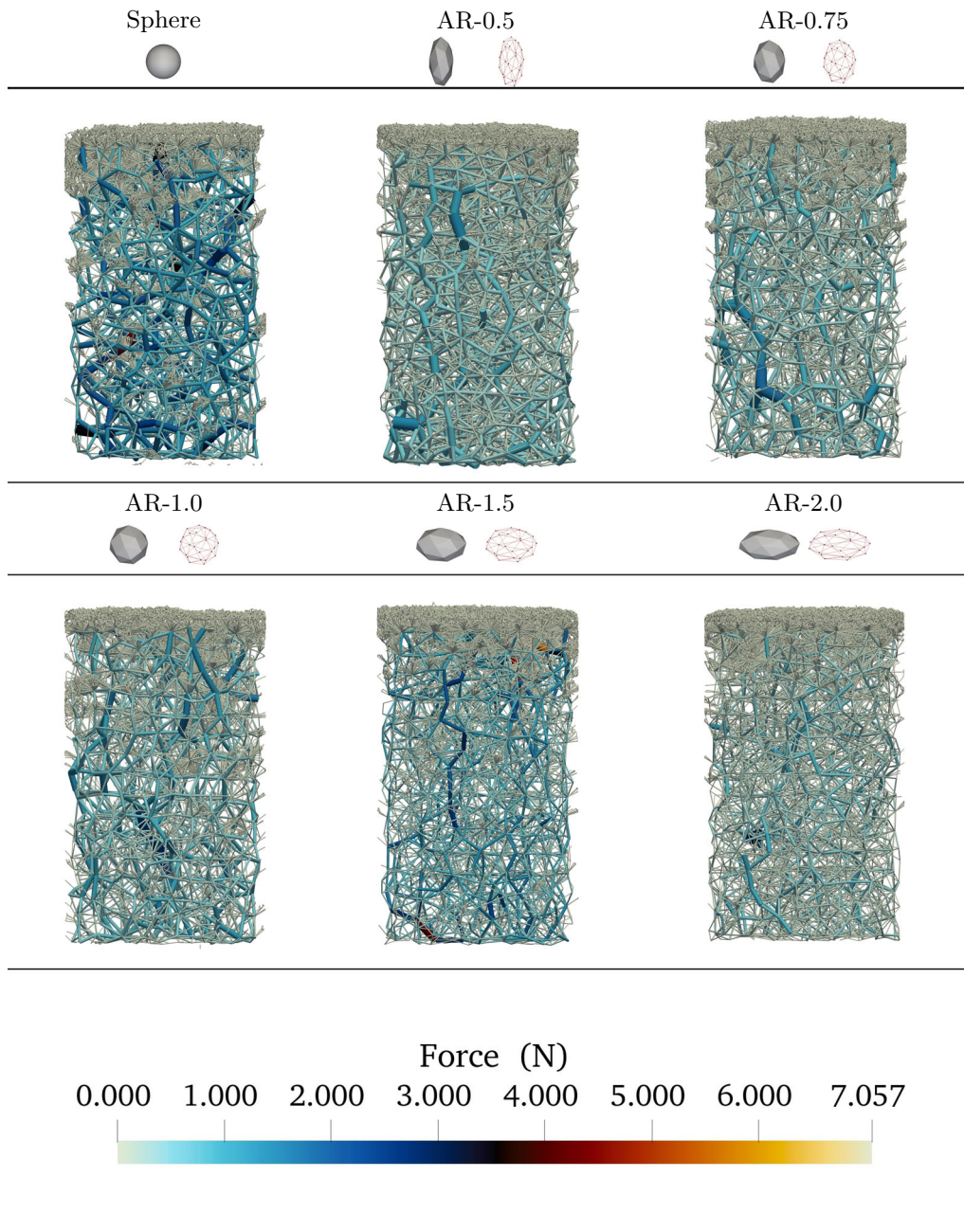
respectively, explaining the macroscopic features from a micromechanical view [22, 65]. The contact force between particles is represented by the connecting tube, where the thickness of the tube is proportional to the magnitude of contact force and the color changes accordingly.

After a given consolidation of 100 kPa, the coarse grains establish a stable normal force network. Contact forces in the soils are mainly transmitted through coarse grains [22]. The strong chains between coarse particles remain the state of equilibrium during simulation, providing stress support for the skeleton under the seepage. Therefore, the weak force chains into clusters between the stagnant fines are the focus. Unlike the uniform and sparse distribution of force chains before accumulating fines, with the transportation of fines carried by fluid under the action of seepage, weak force chains are formed between the clogged fines due to the interparticle contact, thereby reconfiguring the force network. In addition, Table 5 compares the reconfigured

tubular force network after suffusion ($t = 12$ s) for all cases with different shapes. The variation in magnitude and distribution of weak force clusters mirrors the morphology of clogging blocks. As expected, polyhedral fines generate significantly numerous thin chains in accumulation zone, while the dense clusters are not present in weak clogging and loss zone.

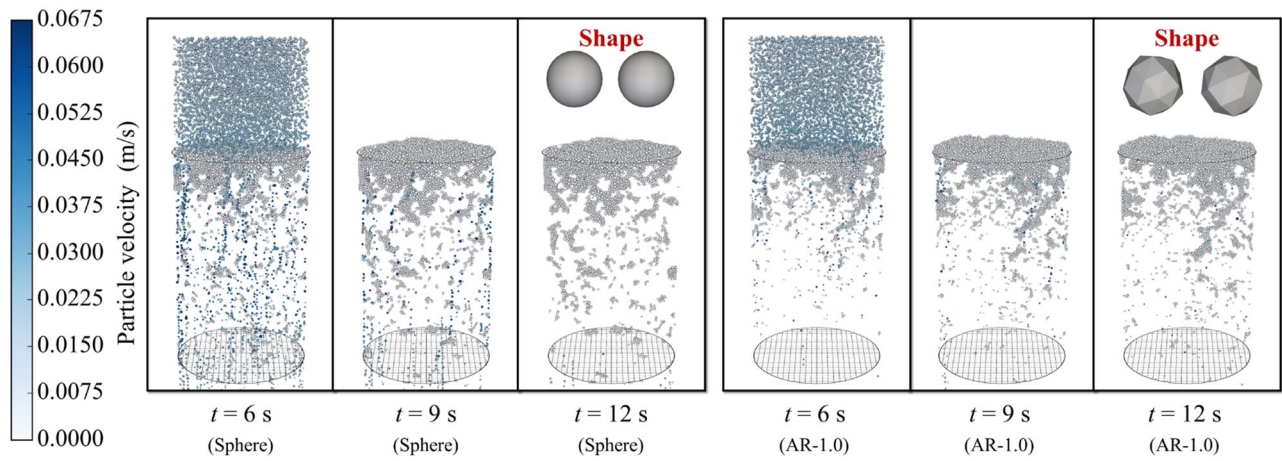
4.5 Evolution of particle and fluid dynamics

The CFD-iDEM algorithm provides superior feasibility for probing the microscopic behavior of fluid–particle system. The shape, size, location and velocity of each particle, as well as fluid velocity and pressure, are extracted, which visualizes the migration and clogging. The spatial distributions with the velocity field of spherical and quasi-spherical cases are depicted in Fig. 24a. It can be observed that the formation of clogging blocks gradually slows down

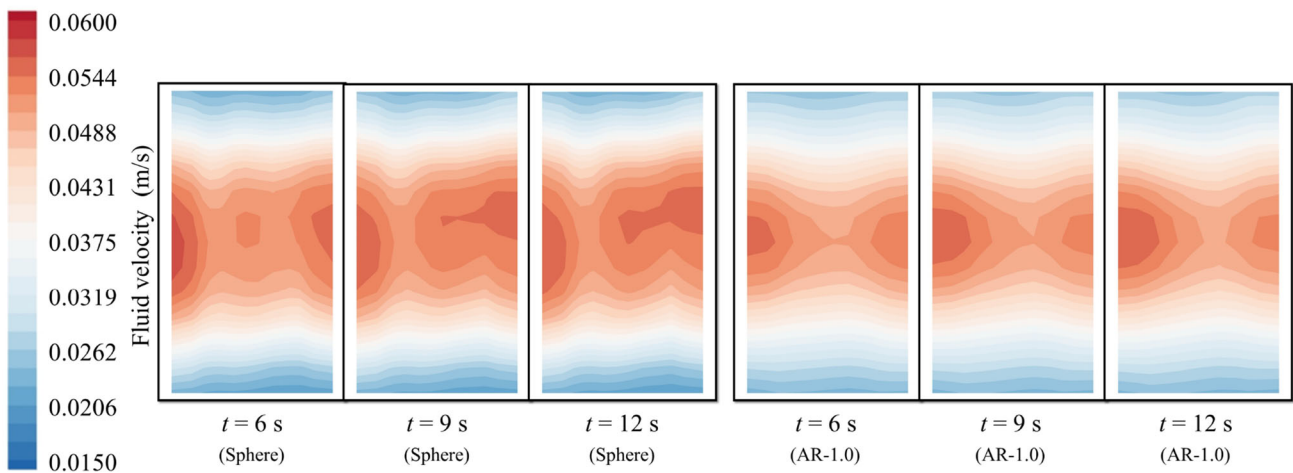
Table 5 Force network after suffusion for all cases

during the simulation. The location and morphology of large agglomerates are basically constructed at 6 s, and the subsequent fine particle replenishes these. Localized clogging occurs, leading to pore constriction and reduced local permeability, which changes the flow patterns in adjacent channels. Deeper (weak clogging and loss zone) with less tendency to this phenomenon of dependent clogging (clogging influenced by nearby clogs). Clogging in porous medium shows a non-random distribution, the dependent

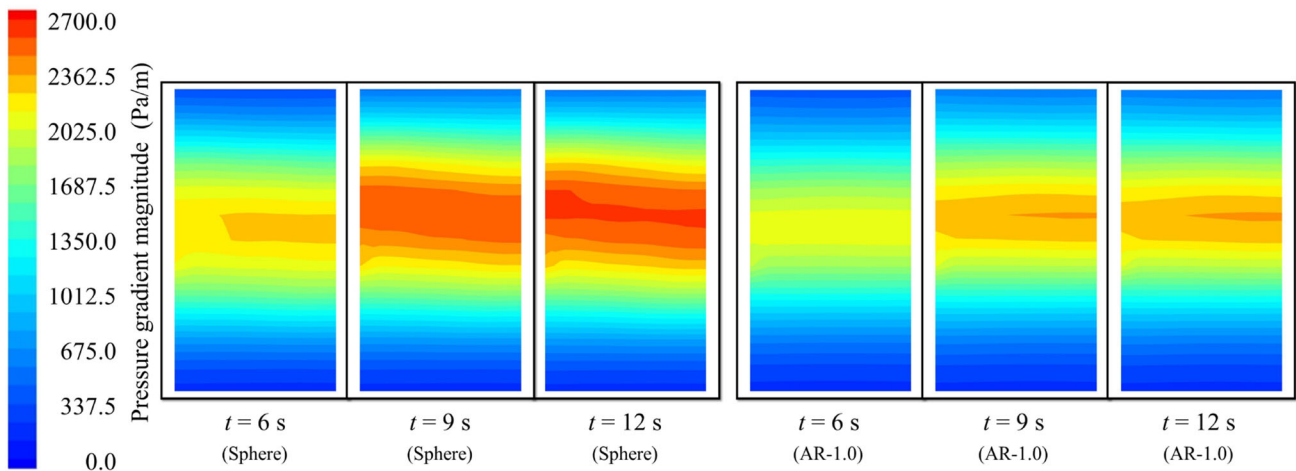
clogging has a more pronounced contribution to the reduction of local permeability than independent clogging [29]. Comparing the spatial distribution in the early stage of suffusion ($t = 6$ s) for two typical cases (the spherical and quasi-spherical), polyhedral fines form more granular clusters with low or zero velocity above the filter plate. On the contrary, spherical particles are rapidly transported deeper under pore water pressure, and at 6 s, erosion of fines out of the coarse-grained skeleton has been



(a) Evolution of spatial distributions with the particle velocity field



(b) Evolution of fluid velocity field on central cutting plane (z -coordinate: $-50 \text{ mm} \sim 50 \text{ mm}$)



(c) Evolution of pressure gradient on central cutting plane (z -coordinate: $-50 \text{ mm} \sim 50 \text{ mm}$)

Fig. 24 Evolution of particle and fluid dynamics: pressure gradient and velocity fields

observed (Fig. 24a). At the end of suffusion ($t = 12 \text{ s}$), 52.46% of polyhedral fines accumulate above the top filter, forming a sizable soil layer. In addition, according to the

particle velocity field, some polyhedral fines still have an obvious seepage velocity at 12 s. This could be attributed to the inadequacy of clusters with limited stability failing

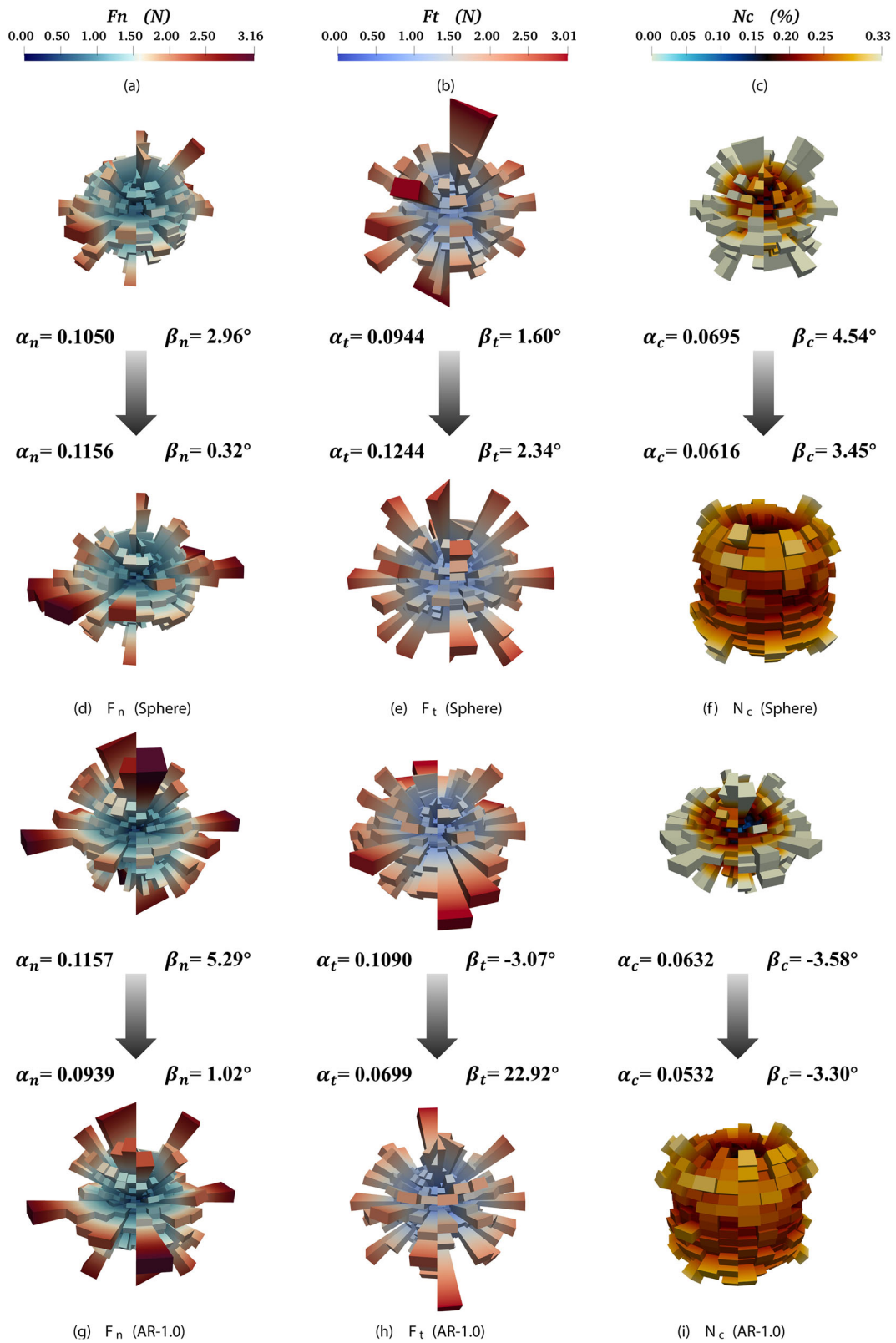


Fig. 25 Orientations of microscopic contact fabric information within the coarse-grained skeleton of sphere and AR-1.0 cases for pre- and post-suffusion

to take the pressure with the accumulation, consequently resulting in particle re-erosion [18]. Figure 24b, c illustrates the dynamic changes in velocity and pressure gradient fields of fluid during suffusion in both spherical and quasi-spherical cases. The fluid velocity is intricately linked to the cross-sectional area of the pore, given that the total fluid flow remains constant [66]. Due to the larger

fluid cell of the unresolved CFD, there is a noticeable transitional zone in the change of fluid velocity and hydraulic gradient within the skeleton, manifesting as significant increases and decreases at the inlet and outlet, respectively. This will result in the impact of fine particle clogging being less pronounced, a challenge that will be addressed in the fully resolved method to be developed

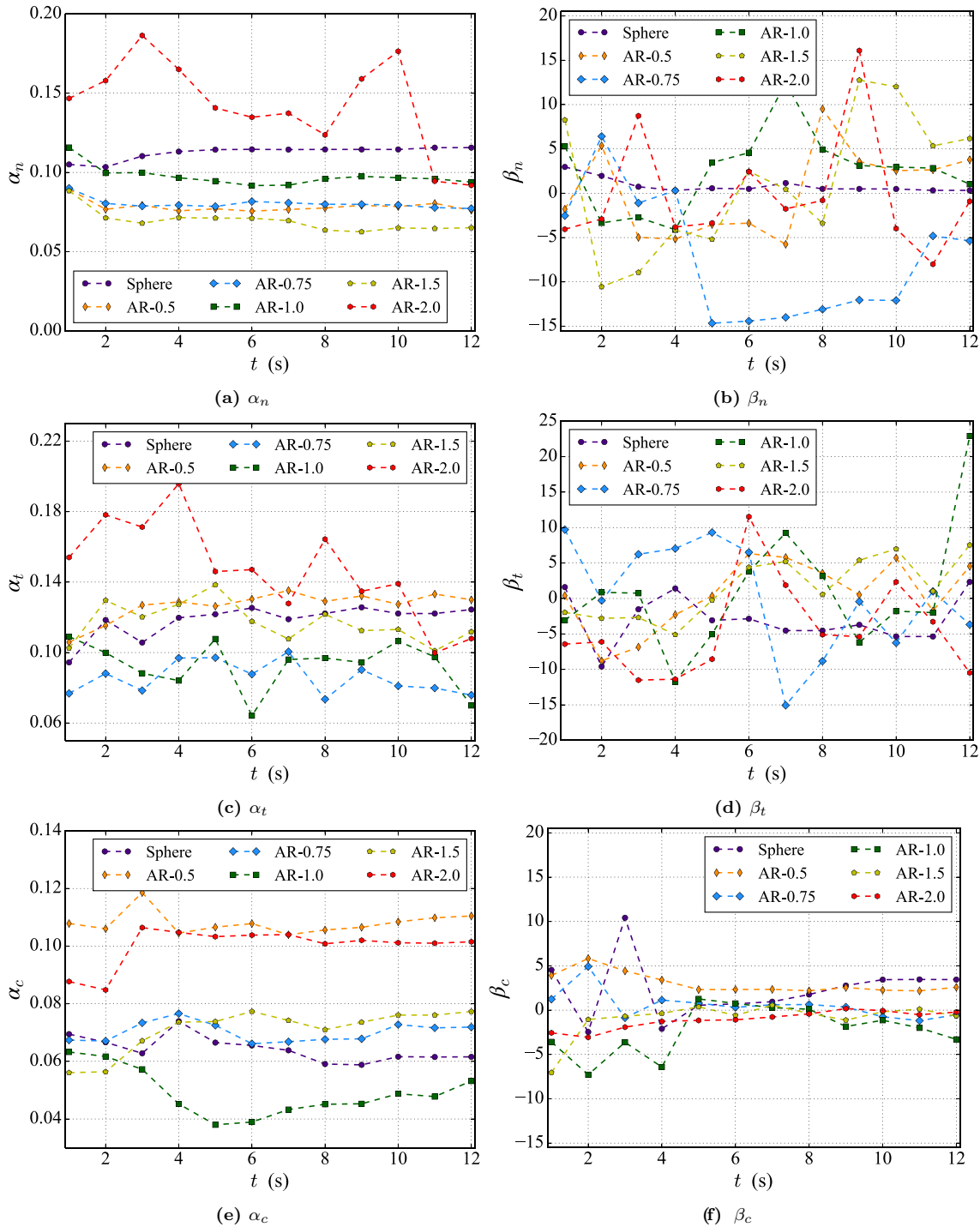


Fig. 26 Evolution of the magnitude and principal direction of anisotropic characteristics during suffusion

further. As suffusion progresses, zones characterized by high velocity and pressure gradient emerge within the skeleton, signifying a reduction of pore space and an intensified clogging effect. Notably, spherical particles contribute to the formation of a broader range and larger values of the impermeable band, owing to the substantial influx into the skeleton (Fig. 14) [7].

4.6 Anisotropic characteristics analysis

The analysis of the contact orientation is important to study the micromechanical characteristics of suffusion [41, 59, 65], the distribution of which can be well-characterized by contact statistics in different angular intervals. It is worth noting that the subsequent anisotropic characteristics is only conducted for the clogging zone. The spatial distributions of the accumulated contact information in the intervals (including the normal contact force F_n , shear contact force F_t and percentages of contact number N_c) are shown in the 3D rose diagram (Fig. 25), which are determined by the following distribution equations:

$$\bar{E}(\varphi) = \frac{1}{2\pi} [1 + \alpha \cos 2(\varphi - \beta)] \quad (22)$$

$$\alpha = 2\sqrt{\left[\int_0^{2\pi} \bar{E}(\varphi) \sin 2\varphi d\varphi \right]^2 + \left[\int_0^{2\pi} \bar{E}(\varphi) \cos 2\varphi d\varphi \right]^2} \quad (23)$$

$$\beta = \frac{1}{2} \arctan \frac{\int_0^{2\pi} \bar{E}(\varphi) \sin 2\varphi d\varphi}{\int_0^{2\pi} \bar{E}(\varphi) \cos 2\varphi d\varphi} \quad (24)$$

where $\int_0^{2\pi} \bar{E}(\varphi) d\varphi = 1$, φ is the polar angle between the force vector and z -axis, α and β define the magnitude and principal direction of anisotropic characteristics (including α_n, β_n for F_n , α_t, β_t for F_t and α_c, β_c for N_c).

The localized clogging clusters are involved in stress transmission to increase both α_n and α_t of the spherical case, which originates from the penetration of detached fines (Fig. 25d, e). The particle shape affects the internal force distribution of the granular skeleton [64], causing greater anisotropy in the normal and shear force for the polyhedral specimen in the initial state. Owing to the shape effects, the clogged fines reduce the orientation preference of polyhedral particles, the magnitude of anisotropy for the three representative parameters of AR-1.0 case decrease after suffusion to tend to be isotropic (Fig. 25g–i). To investigate how the aspect ratio influences the force distribution evolution, Fig. 26 displays the variation in the magnitude and principal direction of anisotropic characteristics during suffusion for various shapes. α_n in polyhedral cases decreases as suffusion progresses, especially with the highest deviation from sphericity, AR-2.0

(Fig. 26a). Likewise, the anisotropy magnitude of the shear contact force experiences significant variation for AR-2.0 (Fig. 26c). In addition, for cases with different shapes, the anisotropy magnitude of the contact number shows noticeable shape effects. The consistently high values of α_c for AR-0.5 and AR-2.0, and the low values for spherical and quasi-spherical cases, suggest that irregular particles with different aspect ratios tend to have a preferred orientation for inter-pore transport or clogging under hydraulic action (Fig. 26e). On the other hand, β_c quickly reaches a steady state, while β_n and β_t fluctuate significantly during the suffusion process. The principal direction of anisotropy of force distribution shows more unstable, reflecting the complex redistribution of stress during the development of particle clogging [64, 65].

5 Summary and conclusions

Particle shape is one of the important factors affecting the migration and clogging of detached fines during suffusion. A discrete element method for generating and testing irregular particle is developed. Subsequently, coupled CFD-iDEM simulations are performed to investigate the shape effects on clogging mechanism of suffusion. The conclusions are drawn employing macro- and micro-analysis.

The behavior of fluid–particle system can be reasonably performed by the coupled method. Compared to the spherical specimen, the polyhedral particles present a non-negligible interlock effect and interparticle occlusion. For identical hydraulic and granular conditions, the polyhedral specimens with different AR values show variability in the degree of accumulation. The higher the degree of deviation from the spherical shape, the more likely it is that polyhedral particles will form particle clusters and local clogging. Quasi-spherical polyhedrons (AR-1.0) are close to spheres in terms of mechanical behavior and pore morphology as opposed to others.

Under the pressure of pore water, spherical particles are quickly carried deeper, while polyhedrons inhibit the transport. In addition, polyhedrons that deviate from a quasi-spherical shape are less susceptible to moving deeper. Distribution and size of clogging clusters decrease gradually with the direction of seepage.

Transmitted particle with a large size, especially polyhedral particle, is more prone to accumulate or be captured. Broad clusters of fines occupy the pore space and form the flow-avoidable caking, preventing the penetration of subsequent particles and promoting the development of clogging. Connectivity of pore space affects clogging progression and local permeability variation. In addition, the evolution in magnitude and distribution of weak force

clusters can mirror the morphology of clogging blocks. The evolution of anisotropic characteristics of force and contact distribution correlates with the development of particle clogging and is influenced by particle shape.

So far, particle shape cannot be ignored in investigation of clogging mechanism. The simulation results obtained in this study emphasize the importance of particle shape in the clogging effects under the action of seepage. Based on this, future investigations can be conducted regarding other granular parameters of irregular particle on clogging during suffusion, such as the angularity, roughness and preferential orientation. Micro-level studies provide sufficient evidence for understanding the mechanical properties of soils. In addition, this study provides an explanation for the macroscopic phenomenon during suffusion in engineering applications, which helps in the control and monitoring of structural facilities to avoid damage.

Acknowledgements This study was financially supported by the National Natural Science Foundation of China (project Nos. 52090084, 52208354 and 51938008), Shenzhen Science and Technology Program (No. KQTD20221101093555006), Research Grants Council of Hong Kong (Nos. 15209119 and 15229223) and the Open Research Project Programme of the State Key Laboratory of Internet of Things for Smart City (University of Macau) (No. SKL-IoTS-C(UM)-2021-2023/ORPF/A16/2022).

Funding Open access funding provided by The Hong Kong Polytechnic University.

Availability of data and materials Data generated or analyzed during this study are available from the corresponding author upon reasonable request.

Declarations

Conflict of interest The authors declare that they have no known competing financial interests or personal relationships that could have appeared to influence the work reported in this paper.

Open Access This article is licensed under a Creative Commons Attribution 4.0 International License, which permits use, sharing, adaptation, distribution and reproduction in any medium or format, as long as you give appropriate credit to the original author(s) and the source, provide a link to the Creative Commons licence, and indicate if changes were made. The images or other third party material in this article are included in the article's Creative Commons licence, unless indicated otherwise in a credit line to the material. If material is not included in the article's Creative Commons licence and your intended use is not permitted by statutory regulation or exceeds the permitted use, you will need to obtain permission directly from the copyright holder. To view a copy of this licence, visit <http://creativecommons.org/licenses/by/4.0/>.

References

- Alem A, Ahfir ND, Elkawafi A, Wang H (2015) Hydraulic operating conditions and particle concentration effects on physical clogging of a porous medium. *Transp Porous Media* 106:303–321
- Allen T (2013) Particle size measurement. Springer
- Chang D (2012) Internal erosion and overtopping erosion of earth dams and landslide dams. Ph.D. thesis
- Chang DS, Zhang LM (2013) Critical hydraulic gradients of internal erosion under complex stress states. *J Geotech Geoenviron Eng* 139:1454–1467
- Chen F, Jiang S, Xiong H, Yin Zy, Chen X (2023) Micro pore analysis of suffusion in filter layer using tri-layer CFD–DEM model. *Comput Geotech* 156:105303
- Chen F, Xiong H, Wang X, Yin ZY (2022) Transmission effect of eroded particles in suffusion using the CFD-DEM coupling method. *Acta Geotech* 18:1–20
- Chen F, Xiong H, Yin ZY, Chen X (2023) Impermeable and mechanical stability of filter cake under different infiltration conditions via CFD-DEM. *Acta Geotech* 1–26
- Cho GC, Dodds J, Santamarina JC (2006) Particle shape effects on packing density, stiffness, and strength: natural and crushed sands. *J Geotech Geoenviron Eng* 132:591–602
- Climent N, Arroyo M, O'Sullivan C, Gens A (2014) Sand production simulation coupling dem with CFD. *Eur J Environ Civ Eng* 18:983–1008
- Du X, Ye X, Zhang X (2018) Clogging of saturated porous media by silt-sized suspended solids under varying physical conditions during managed aquifer recharge. *Hydrol Process* 32:2254–2262
- Fannin R, Slangen P (2014) On the distinct phenomena of suffusion and suffosion. *Géotechnique Letters* 4:289–294
- Font-Capo J, Pujades E, Vázquez-Suñé E, Carrera J, Velasco V, Montfort D (2015) Assessment of the barrier effect caused by underground constructions on porous aquifers with low hydraulic gradient: A case study of the metro construction in barcelona, Spain. *Eng Geol* 196:238–250
- Gan J, Yu A (2020) Dem study on the packing density and randomness for packing of ellipsoids. *Powder Technol* 361:424–434
- Gan J, Yu A, Zhou Z (2016) Dem simulation on the packing of fine ellipsoids. *Chem Eng Sci* 156:64–76
- Garcia A, Aboufoul M, Asamoah F, Jing D (2019) Study the influence of the air void topology on porous asphalt clogging. *Constr Build Mater* 227:116791
- Gerber G, Rodts S, Aïmeidieu P, Faure P, Coussot P (2018) Particle-size-exclusion clogging regimes in porous media. *Phys Rev Lett* 120:148001
- Guo C, Cui Y (2020) Pore structure characteristics of debris flow source material in the Wenchuan earthquake area. *Eng Geol* 267:105499
- Hafez A, Liu Q, Finkbeiner T, Alouhali RA, Moellendick TE, Santamarina JC (2021) The effect of particle shape on discharge and clogging. *Sci Rep* 11:1–11
- Hertz H (1896) Über die berührung fester elastischer körper (on the contact of elastic solids). *J reine und angewandte mathematik* 92:156. Miscellaneous papers H. Hertz. Macmillan, London
- Hosn RA, Sibille L, Benahmed N, Chareyre B (2018) A discrete numerical model involving partial fluid-solid coupling to describe suffusion effects in soils. *Comput Geotech* 95:30–39
- Hu Z, Yang Z, Zhang Y (2020) CFD–DEM modeling of suffusion effect on undrained behavior of internally unstable soils. *Comput Geotech* 126:103692
- Hu Z, Zhang Y, Yang Z (2019) Suffusion-induced deformation and microstructural change of granular soils: a coupled CFD-DEM study. *Acta Geotech* 14:795–814
- Huilin L, Gidaspow D (2003) Hydrodynamics of binary fluidization in a riser: CFD simulation using two granular temperatures. *Chem Eng Sci* 58:3777–3792

24. Hunter R, Bowman E (2018) Visualisation of seepage-induced suffusion and suffusion within internally erodible granular media. *Géotechnique* 68:918–930
25. Ke L, Takahashi A (2012) Strength reduction of cohesionless soil due to internal erosion induced by one-dimensional upward seepage flow. *Soils Found* 52:698–711
26. Kenney T, Lau D (1986) Internal stability of granular filters: reply. *Can Geotech J* 23:420–423
27. Kloss C, Goniva C, Hager A, Amberger S, Pirker S (2012) Models, algorithms and validation for opensource dem and CFD-DEM. *Progress Comput Fluid Dyn Int J* 12:140–152
28. Li Y, Zhang J, Fan LS (1999) Numerical simulation of gas-liquid-solid fluidization systems using a combined CFD-VOF-DPM method: bubble wake behavior. *Chem Eng Sci* 54:5101–5107
29. Liu Q, Zhao B, Santamarina JC (2019) Particle migration and clogging in porous media: a convergent flow microfluidics study. *J Geophys Res Solid Earth* 124:9495–9504
30. Liu Y, Wang L, Hong Y, Zhao J, Yin ZY (2020) A coupled CFD-DEM investigation of suffusion of gap graded soil: coupling effect of confining pressure and fines content. *Int J Numer Anal Methods Geomech* 44:2473–2500
31. Lu Z, Yao A, Su A, Ren X, Liu Q, Dong S (2019) Re-recognizing the impact of particle shape on physical and mechanical properties of sandy soils: a numerical study. *Eng Geol* 253:36–46
32. Marin A, Lhuissier H, Rossi M, Kähler CJ (2018) Clogging in constricted suspension flows. *Phys Rev E* 97:021102
33. Maroof MA, Mahboubi A, Noorzad A (2020) A new method to determine specific surface area and shape coefficient of a cohesionless granular medium. *Adv Powder Technol* 31:3038–3049
34. Maroof MA, Mahboubi A, Noorzad A (2021) Effects of grain morphology on suffusion susceptibility of cohesionless soils. *Granul. Matter* 23:1–20
35. Mitchell JK, Soga K et al (2005) *Fundamentals of soil behavior*, vol 3. Wiley, New York
36. Nguyen CD, Benahmed N, Andò E, Sibille L, Philippe P (2019) Experimental investigation of microstructural changes in soils eroded by suffusion using x-ray tomography. *Acta Geotech* 14:749–765
37. Nguyen TT, Indraratna B (2020) The role of particle shape on hydraulic conductivity of granular soils captured through Kozeny–Carman approach. *Géotech Lett* 10:398–403
38. Nian Tk WuH, Takara K, Li Dy, Yj Zhang (2021) Numerical investigation on the evolution of landslide-induced river blocking using coupled DEM-CFD. *Comput Geotech* 134:104101
39. Peng Y, Yin ZY (2023) Micromechanical analysis of suction pile-granular soil interaction under inclined pulling load of mooring line: Mooring depth effect. *Mar Struct* 92:103499
40. Pujades E, López A, Carrera J, Vázquez-Suñé E, Jurado A (2012) Barrier effect of underground structures on aquifers. *Eng Geol* 145:41–49
41. Qian JG, Zhou C, Yin ZY, Li WY (2021) Investigating the effect of particle angularity on suffusion of gap-graded soil using coupled CFD-DEM. *Comput Geotech* 139:104383
42. Ren DJ, Shen SL, Cheng WC, Zhang N, Wang ZF (2016) Geological formation and geo-hazards during subway construction in Guangzhou. *Environ Earth Sci* 75:1–14
43. Rochim A, Marot D, Sibille L et al (2017) Effects of hydraulic loading history on suffusion susceptibility of cohesionless soils. *J Geotech Geoenviron Eng* 143:04017025
44. Sato M, Kuwano R (2015) Suffusion and clogging by one-dimensional seepage tests on cohesive soil. *Soils Found* 55:1427–1440
45. Sezer Gİ, Ramyar K, Karasu B, Göktepe AB, Sezer A (2008) Image analysis of sulfate attack on hardened cement paste. *Mater Des* 29:224–231
46. Sibille L, Marot D, Sail Y (2015) A description of internal erosion by suffusion and induced settlements on cohesionless granular matter. *Acta Geotech* 10:735–748
47. Slangen P, Fannin R (2017) The role of particle type on suffusion and suffusion. *Géotech Lett* 7:6–10
48. Tang Y, Chan DH, Zhu DZ (2017) A coupled discrete element model for the simulation of soil and water flow through an orifice. *Int J Numer Anal Methods Geomech* 41:1477–1493
49. Taylor CJ, Kriegman DJ (1994) Minimization on the lie group SO(3) and related manifolds
50. Torskaya T, Shabro V, Torres-Verdín C, Salazar-Tio R, Revil A (2014) Grain shape effects on permeability, formation factor, and capillary pressure from pore-scale modeling. *Transp Porous Media* 102:71–90
51. Tsuji Y, Tanaka T, Ishida T (1992) Lagrangian numerical simulation of plug flow of cohesionless particles in a horizontal pipe. *Powder Technol* 71:239–250
52. Wadell H (1932) Volume, shape, and roundness of rock particles. *J Geol* 40:443–451
53. Wan CF, Fell R (2008) Assessing the potential of internal instability and suffusion in embankment dams and their foundations. *J Geotech Geoenviron Eng* 134:401–407
54. Wang P, Yin ZY (2022) Effect of particle breakage on the behavior of soil-structure interface under constant normal stiffness condition with dem. *Comput Geotech* 147:104766
55. Wang T, Wang P, Yin zy, Zhang F (2022) DEM-DFM modeling of suffusion in calcareous sands considering the effect of double-porosity. *Comput Geotech* 151:104965
56. Wang X, Huang B, Tang Y, Hu T, Ling D (2022) Microscopic mechanism and analytical modeling of seepage-induced erosion in bimodal soils. *Comput Geotech* 141:104527
57. Wang X, Zy Yin, Jq Zhang, Xiong H, Su D (2021) Three-dimensional reconstruction of realistic stone-based materials with controllable stone inclusion geometries. *Constr Build Mater* 305:124240
58. Wang XW, Xu YS (2023) Permeability property variation in sandy soil induced by suffusion via a horizontal seepage laboratory test. *Acta Geotech* 1–14
59. Wautier A, Bonelli S, Nicot F (2018) Flow impact on granular force chains and induced instability. *Phys Rev E* 98:042909
60. Wautier A, Bonelli S, Nicot F (2019) Dem investigations of internal erosion: grain transport in the light of micromechanics. *Int J Numer Anal Methods Geomech* 43:339–352
61. Won J (2022) Assessment of internal stability of sand-fine mixture using particle detachment model and its implications on suffusion. *Acta Geotech* 17:4667–4680
62. Xiong H, Qiu Y, Liu J, Yin ZY, Chen X (2023) Macro-microscopic mechanism of suffusion in calcareous sand under tidal fluctuations by coupled CFD-DEM. *Comput Geotech* 162:105676
63. Xiong H, Sun J, Chen F, Yin ZY, Chen X (2023) Suffusion behavior of crushed calcareous sand under reversed cyclic hydraulic conditions. *Constr Build Mater* 408:133817
64. Xiong H, Wu H, Bao X, Fei J (2021) Investigating effect of particle shape on suffusion by CFD-DEM modeling. *Constr Build Mater* 289:123043
65. Xiong H, Yin ZY, Zhao J, Yang Y (2021) Investigating the effect of flow direction on suffusion and its impacts on gap-graded granular soils. *Acta Geotech* 16:399–419
66. Xiong H, Zhang Z, Bao X, Wu H, Yin Zy, Chen X (2024) Micro-mechanical analysis of particle shape effect on suffusion of gap-graded soils. *Comput Geotech* 165:105925
67. Xiong H, Zhang Z, Sun X, Yin Zy, Chen X (2022) Clogging effect of fines in seepage erosion by using CFD-DEM. *Comput Geotech* 152:105013

68. Xiong H, Zhang Z, Yang J, Yin Zy, Chen X (2023) Role of inherent anisotropy in infiltration mechanism of suffusion with irregular granular skeletons. *Comput Geotech* 162:105692
69. Yang J, Buettner KE, DiNenna VL, Curtis JS (2022) Computational and experimental study of the combined effects of particle aspect ratio and effective diameter on flow behavior. *Chem Eng Sci* 255:117621
70. Yang J, Yin ZY (2021) Soil-structure interface modeling with the nonlinear incremental approach. *Int J Numer Anal Methods Geomech* 45:1381–1404
71. Yang J, Yin ZY, Laouafa F, Hicher PY (2019) Modeling coupled erosion and filtration of fine particles in granular media. *Acta Geotech* 14:1615–1627
72. Yang J, Yin ZY, Laouafa F, Hicher PY (2020) Three-dimensional hydromechanical modeling of internal erosion in dike-on-foundation. *Int J Numer Anal Methods Geomech* 44:1200–1218
73. Ye X, Cui R, Du X, Ma S, Zhao J, Lu Y, Wan Y (2019) Mechanism of suspended kaolinite particle clogging in porous media during managed aquifer recharge. *Groundwater* 57:764–771
74. Yin ZY, Wang P, Zhang F (2020) Effect of particle shape on the progressive failure of shield tunnel face in granular soils by coupled FDM-DEM method. *Tunn Undergr Space Technol* 100:103394
75. Zhang D, Zhang X, Du W (2022) Dem-fem based numerical analysis on mechanical responses of sandy soil and pipeline to seepage erosion. *Eng Geol* 310:106868
76. Zhang J, She R, Dai Z, Ming R, Ma G, Cui X, Li L (2018) Experimental simulation study on pore clogging mechanism of porous pavement. *Constr Build Mater* 187:803–818
77. Zhao B, O’Sullivan C (2022) Fluid particle interaction in packings of monodisperse angular particles. *Powder Technol* 395:133–148
78. Zhao S, Zhou X, Liu W (2015) Discrete element simulations of direct shear tests with particle angularity effect. *Granul Matter* 17:793–806

Publisher’s Note Springer Nature remains neutral with regard to jurisdictional claims in published maps and institutional affiliations.